

Structural insights into the gating mechanism of human Cx43/GJA1 gap junction channel

Jae-Sung Woo (✉ jaesungwoo@korea.ac.kr)

Korea University

Hyuk-Joon Lee

Korea University <https://orcid.org/0000-0001-7568-2307>

Hyung Jin Cha

Korea University

Hyeongseop Jeong

Korea Basic Science Institute

Seu-Na Lee

Korea University

Chang-Won Lee

Korea University

Minsoo Kim

Sungkyunkwan University

Jejoong Yoo

Sungkyunkwan University

Article

Keywords: cryo-EM, gap junction intercellular channel, gating mechanism, conformational change, N-terminal helix, pore size, ion selectivity, π -helix

Posted Date: July 26th, 2021

DOI: <https://doi.org/10.21203/rs.3.rs-730129/v1>

License:   This work is licensed under a Creative Commons Attribution 4.0 International License.

[Read Full License](#)

Version of Record: A version of this preprint was published at Nature Communications on February 18th, 2023. See the published version at <https://doi.org/10.1038/s41467-023-36593-y>.

Abstract

Connexin family proteins assemble into hexameric hemichannels in a cell membrane, which dock together between two adjacent membranes to form gap junction intercellular channels (GJICs). The most ubiquitously expressed connexin Cx43 plays important roles in numerous biological processes. Here we report cryo-EM structures of Cx43 GJICs at 3.1–3.6 Å resolutions, which show dynamic conformational changes of N-terminal helices (NTHs) caused by pH change or C-terminal truncation. Cx43 GJICs in a channel-closing condition contain 12 protomers in gate-covering NTH (GCN) conformation, while those in opening conditions have varying compositions of GCNs and pore-lining NTHs (PLNs) resulting in various pore dimensions and electrostatic surface potentials. GCN-to-PLN transition accompanies π -helix formation in the first transmembrane helix (TM1), movement of TM2-4 that creates a side opening to the membrane, and structural stabilization of the cytoplasmic loop. Our study provides structural insights into the intercellular ion/metabolite transfer and the lateral lipid transport through Cx43 GJIC.

Introduction

Gap junction intercellular channels (GJICs), which facilitate direct communication between apposed cells play important roles in various biological processes such as cardiac contraction, electrical coupling, and cell differentiation and death¹. GJIC is formed by docking of two opposed hemichannels (also called connexons) from adjacent cells²⁻⁸, and each hemichannel is composed of six connexin (Cx) protomers⁹. In humans, 21 connexin genes have been found and categorized into A to E classes based on amino acid sequence similarity. Compared with other membrane channels, GJICs have relatively large pores for the passage of ions and metabolites, which enable large-area intercellular communication in various tissues^{10,11}.

Cx43, also known as GJA1, is the most ubiquitously expressed connexin. It is detected in most cell types and thus involved in numerous biological processes. For example, it is the most abundant connexin in cardiomyocytes, bone cells, skins, and astrocytes, and plays crucial roles in synchronized contraction of the heart¹², bone mass regulation via mechanotransduction¹³⁻¹⁵, maintaining the integrity of avascular epidermis¹⁶, and coordinating central nervous system (CNS) activities¹⁷. Cx43 is also implicated in long-range intercellular communication through tunneling nanotubes and extracellular vesicles¹⁸.

Many Cx43-related human diseases have been studied, highlighting the biomedical importance of Cx43. A number of mutations in the *Cx43* gene have been found to cause developmental disorders such as oculodentodigital dysplasia (ODDD), palmoplantar keratoderma (PPK), and heart malformations^{16,19,20}. Upregulated Cx43 expression may be associated with Alzheimer's disease, Parkinson's disease, and various cancers²¹⁻²⁵. In brain cancer, carcinoma cells utilize increased Cx43 GJIC formation with astrocytes to transport cyclic GMP-AMP, thus promoting brain metastasis²⁴. Arrhythmia and Keratitis-ichthyosis-deafness (KID) are also related to Cx43²⁶.

The gating and permeability of Cx43 GJICs are known to be regulated by many factors such as transjunctional voltage (V_j), pH, divalent ions, interacting proteins, reactive oxygen-nitrogen species, phosphorylation, and membrane lipids²⁷⁻²⁹. In altered intracellular conditions including acidic pH and elevated calcium levels, often induced by ischemia, Cx43-mediated gap junctional conductance is inhibited, increasing the likelihood of cardiac arrhythmia³⁰. With a threefold increased intracellular calcium level, Cx43-mediated gap junctional conductance is also decreased by 95% in a calcium-calmodulin dependent manner³¹. In hypercholesterolemic conditions, decreased conduction velocity of Cx43 GJICs in the myocardium was observed¹².

Although the gating mechanism of Cx43 GJICs is not clearly understood yet, mutational studies have suggested that its N-terminal helix (NTH) plays a critical role in channel gating and charge selectivity. Mutations of two conserved residues (W4A and ODDD-linked L7V) in the NTH greatly diminished dye transfer activity and junctional conductance of Cx43 GJICs³². A heteromeric GJIC containing both wild-type and W4Y mutant protomers also showed 10-fold decreased junctional conductance³³. A double mutation of D12S and K13G dramatically reduced voltage-dependent gating property of GJICs³⁴.

The GJIC structure for a Cx43 mutant with deletion of C-terminal 119 residues was determined with electron cryo-crystallography in 1999 at very low resolution^{4,35}, providing structural insights into the packing arrangement of 12 transmembrane domains (TMDs) and the docking of two hemichannels. A crystal structure of Cx26 GJIC reported in 2009⁵ revealed an overall dodecameric architecture and detailed intermolecular interactions of connexin protomers composed of NTHs, TMDs and extracellular loops (ECLs). Although this structure showed that NTHs lined the pore inside through the interactions with the first transmembrane helices (TM1s) and TM2s, weak electron density for NTHs has indicated their high flexibility and limited our understanding of detailed interactions between NTHs and TM helices. Recent cryo-EM structures of Cx46/Cx50 GJIC⁷ showed that W4 and L7 residues of NTHs, which are highly conserved in the connexin family, tightly bound to the hydrophobic grooves formed by TM1s and TM2s. Through these interactions, NTHs constrict the pore with a solvent-accessible diameter of 11 Å and the hydrophobic groove formed by TM1 and TM2 is masked by NTHs, resulting in a hydrophilic pore pathway, based on which the structure has been regarded as completely open state of GJICs. While the structures of GJICs in the closed state are not yet determined at high-resolution, several low-resolution structures of Cx26 GJICs closed by M34A mutation or acidic pH has shown a large density blob of NTHs blocking the pore pathway, suggesting that NTHs could function as physical plugs³⁶⁻³⁸. Recently, we determined the cryo-EM structure of Cx31.3 hemichannel⁹ which shows a narrower pore (~8 Å diameter) formed by six NTHs horizontally covering the cytoplasmic gate. However, it is still unclear whether GJICs and other hemichannels also adopt this NTH conformation to downregulate the channel activity.

Cx43 has an ~40 amino-acid cytoplasmic loop (CL) and ~150 amino-acid C-terminal loop (CTL), which play important roles in pH gating, post-translational modifications and protein-protein interactions²⁷. While Cx43 GJIC exhibits the maximum H⁺ transmission at pH ~6.9, the transmission activity decreases

sharply with lowering or rising pH until complete closure of the channel at pH 6.4 or 7.6^{39,40}. A Cx43 derivative with deletion of residues from K258 to the C-terminus (Cx43-M257) is constitutively open at least in the pH range from 6.4 to 7.6⁴⁰⁻⁴².

Here we determined cryo-EM structures of wild-type Cx43 (Cx43-WT) GJICs at different pHs (pH 6.9 and 8.0) and Cx43-M257 GJICs at pH 8.0, revealing the conformational change of Cx43 by increased pH or C-terminal deletion. The detailed structural comparison between two different conformations of Cx43 reveals substantial conformational changes in not only NTHs but also TM helices and CL, including π -helix formation in the middle of TM1. Our conformational variation analyses focused on individual protomers identified various compositions of two different protomer conformations in Cx43 GJICs at pH 6.9, the condition leading to channel opening. Dye transfer assays and molecular dynamics (MD) simulations showed that the conformational change is crucial for the transport of molecules larger than ATP and the regulation of ion selectivity, respectively. We also found that the conformational changes open and close a small gap between two neighboring TMDs possibly for the export of lipids remaining inside the pore. These findings suggest that the size and surface property of the pore pathway are regulated by individual conformational changes of NTHs, and the gating mechanism includes not only the conformational changes of NTHs in the cytoplasmic gate but also that of TMDs allowing the movement of lipid molecules in and out of the pore.

Results

Purification and structure determination of Cx43 GJICs.

To understand the gating mechanism of GJICs, high resolution structures in both open and closed states are necessary. Since previously reported high resolution structures of other GJICs showed similar conformations of NTHs and TMDs which are thought to represent the open state, we first aimed to solve the structure in the closed state. Based on previous electrophysiological studies⁴⁰ showing that Cx43 GJICs is inactive above pH 7.6 or below pH 6.4, we expressed human Cx43-WT using human embryonic kidney 293 EBNA (HEK293E) cells and purified the protein at pH 8.0 in a buffer containing lauryl maltose neopentyl glycol (LMNG) and cholesteryl hemisuccinate (CHS). Subsequent treatment with lambda-phosphatase⁴³ and a universal deubiquitinase DUB (M48)⁴⁴ was necessary to overcome problems with sample heterogeneity (Extended Data Fig. 1a,b). Purified protein was concentrated to 1.4 mg/ml to increase the ratio of GJICs to hemichannel. The improved Cx43 sample dramatically reduced biased particle orientation in EM grids and yielded a final EM map of Cx43-WT GJICs with D6 symmetry at 3.1 Å resolution (Fig. 1a,b, and Extended Data Figs. 1d and 2a,d, and Table 1).

The final structural model contains NTHs, TMDs and ECLs (Fig. 1c,d), but not CLs and CTLs, which remained unresolved due to poor EM density. In addition, since the map density for N-terminal methionine (M1) was completely invisible, we investigated N-terminal modification using mass spectrometric analysis. The results showed that Met1 was not detected at all, and the following G2 residue was partially

acetylated (Extended Data Fig. 1c). This modification pattern of Cx43 is similar with that of Cx31.3 expressed in the same human cell line⁹. However, we could not identify the acetylation state of G2 from the cryo-EM data due to the ambiguous map density of this position, and therefore included non-acetylated G2 in our final model.

The resolution for the extracellular region of the structural model (2.8-3.1 Å) was higher than that for the cytoplasmic region (3.7-4.0 Å) (Extended Data Fig. 2a), consistent with previously determined GJCh structures. In addition, as previously observed in the Cx31.3 hemichannel structure at 2.3 Å⁹, the Cx43 GJCh structure had many clear density features corresponding to water molecules in the extracellular region (Fig. 1a,b). We also found several long densities surrounding TMDs, which likely correspond to detergents, and thus modeled acyl chains into the densities (Fig. 1b,d). More acyl chains were ordered at the outer leaflet than the inner, and this phenomenon is consistent with that in the Cx46/50 GJCh structure in lipid nanodiscs at 1.9 Å⁸.

Cx43-WT GJCh at pH ~8.0 adopts the gate-covering NTH (GCN) conformation.

Since NTHs are located inside the GJCh pore, they always form a constriction site, the pore region with the minimum diameter. In the structure of Cx43-WT GJCh at pH ~8.0, six NTHs in each connexon adopt the gate-covering NTH (GCN) conformation which is similar with that of the Cx31.3 hemichannel structure and different from the pore-lining NTH (PLN) conformations of previous Cx26 and Cx46/50 GJCh structures (Extended Data Fig. 3a). The constriction diameter determined by the six N-termini facing toward the pore center had a solvent accessible diameter of ~7 Å (Fig. 1b), which is smaller than the hydrodynamic diameter of ATP (~9.8 Å)⁴⁵ and the diameters of the constricted pore regions in available hemichannel or GJCh structures. Therefore, this conformation likely represents a closed state at least for large metabolites such as ATP. However, because of the ~7 Å pore diameter, it is still unclear how ion transfer is completely blocked at pH >7.6 by this conformation. One possibility is that the pore may contain disordered lipids/detergents inside that we are unable to resolve in our EM maps (Fig. 2a).

The GCN conformation of Cx43 GJCh is mainly stabilized by the intramolecular interactions of NTH with TM2, as we also observed in the previous Cx31.3 hemichannel structure. L10 and V14 of the NTH participate in intramolecular hydrophobic interactions with Y92, L93, V96, F97, and M100 of TM2 (Fig. 2b). These residues are hydrophobically conserved (>80%) in connexin A and C classes, supporting the previous idea that GJChs in A and C classes may have similar GCN conformations⁹ (Fig. 2c). In contrast, we could not find any close intermolecular interaction between NTH and TM2 except a salt bridge between D12 and R101 or any significant interaction between neighboring NTHs except an ionic interaction of D3 with the N-terminal amino group (Extended Data Fig. 3b).

We found significant structural differences between GCN conformations of Cx43 and Cx31.3. First, a superposition of Cx43 GJCh and Cx31.3 hemichannel led to poor alignment of TM2 and the NTH, in contrast to TM1 (Extended Data Fig. 3c). In particular, the cytoplasmic end of TM2 in Cx43 is ~6 Å away from the pore center compared to that of Cx31.3 (Extended Data Fig. 3d). Second, the interaction

networks between hydrophobic amino acid residues differ significantly. For example, in Cx31.3, F5 of NTH closely interacts with L96 of TM2, whereas the corresponding residues of Cx43 (A6 and M100) are distant from each other (Fig. 2b and Extended Data Fig. 3d). This conformational difference results in a large hole between two neighboring NTHs and TM2 at the cytoplasmic gate of Cx43 GJICH. Notably, this hole is filled with unidentified density features that we attribute to partially resolved detergent or lipid molecules (Figs. 1d, 2a and 2d). In addition, the map densities presumed to be CHS added during purification were also found in a deep hydrophobic pocket between NTH, TM1 and TM2 (Figs. 1d, 2a, 2d and 2e). These lipids bound to NTH, TM1, and/or TM2 of Cx43 likely contribute to stabilization of the GCN conformation by masking solvent-exposed hydrophobic surfaces.

To rule out the possibility that the GCN conformation is an artifact caused by detergents, Cx43 GJICH was reconstituted in lipid nanodiscs at pH 8.0 and the structure was determined at 3.6 Å (Fig. 1e, and Extended Data Fig. 1e and 2b, and Table 1). Although the resolution was not as high as that in detergents, it was sufficient to confirm that the overall structure, including the NTH conformation, was almost identical to that in LMNG/CHS environment (Fig. 1e). In addition, this structure also showed strong map densities (presumed to be phospholipids and CHS) filling the gap between NTHs and the deep hydrophobic pocket, respectively (Fig. 1e).

Cx43-M257 GJICHs have various compositions of two different protomer conformations.

To visualize the structure of the Cx43 GJICH in the open state, we purified Cx43-M257 GJICH that is reported to be constitutively open⁴⁰, and analyzed it by cryo-EM (Methods). During the initial 3D classification with no imposed symmetry, we found two prominent classes, one with a clearly visible NTH and the other with an ambiguous one (data not shown). We attributed this to the latter class possibly having varying NTH conformations, and therefore performed a protomer-based conformational variation analysis using single-subunit-focused 3D classification (Fig. 3a and Methods)⁴⁶. The result showed that three classes (classes 3, 4, and 8) were in the PLN conformation, while the remaining five were in the GCN conformation (Fig. 3a). Next, we traced back the GJICH particles to which the protomers in classes 3, 4, and 8 originally belonged, and examined the distribution of how many PLN protomers (protomers in the PLN conformation) were included in each GJICH particle. We found that GJICH particles (59,789 particles) had various PLN:GCN compositions from 0:12 (fully GCN GJICH, 2,183 particles, 3.7%) to 12:0 (fully PLN GJICH, one particle) (Fig. 3b). The number of GJICH particles with three PLN protomers was the largest (12,083 GJICH particles, 20.2%), and >70% particles contained 2-5 PLN protomers, suggesting that these particles might represent open states. Alternatively, the dynamic equilibrium between PLN and GCN states of individual protomers may be required for GJICH to be open.

It should be noted that two protomer classes (classes 4 and 8) have map densities of NTH in both GCN and PLN conformations (Fig. 3a). Therefore, the actual number of PLN protomers in the 3D classification data should be less than the number of protomers in classes 3, 4, and 8 (~30%) and may be close to that in classes 3 and 4 (~20%). Therefore, we also produced another distribution graph with only classes 3

and 4, which showed that fully PLN GJICH was not found and ~67% GJICH particles contain 2-5 PLN protomers (Fig. 3b).

Next, we suspected that some GJICH particles may have PLN protomers in the cryo-EM data of Cx43-WT GJICH at pH ~8, and thus we performed the same analysis with the Cx43-WT data. However, no protomer class with the PLN conformation appeared in the single-subunit-focused 3D classification (Extended Data Fig. 1d), suggesting that the partial deletion of CTL activated the GCN-to-PLN transition of Cx43.

Structure of Cx43-M257 GJICH composed of two different hemichannels in fully PLN and fully GCN conformations, respectively.

Since the majority of connexins in the Cx43-M257 dataset were in the GCN state, we could determine the structure of fully GCN GJICH at 3.2 Å, confirming that it is almost identical with the Cx43-WT GJICH structure (data not shown). However, it was not easy to solve any structures containing PLN protomers at high resolution, because it was difficult to accurately detect and classify the conformational changes of small NTHs in each GJICH particle. The most feasible scenario was likely to solve the structure of GJICH containing one hemichannel with six GCN protomers (fully GCN hemichannel) and the other hemichannel with six PLN protomers (fully PLN hemichannel), because the highest possible symmetry C₆ can be imposed in the 3D reconstruction process. To this end, we performed “focused 3D classification and localized reconstruction” on hemichannels (Methods) and obtained one hemichannel class (Class 6, 7.3%) in fully PLN conformation (Extended Data Fig. 4d). With 8,046 hemichannel sub-particles in this class, we could determine fully PLN hemichannel structure with C₆ symmetry at 4.3 Å (Extended Data Fig. 4e). 3D reconstruction was also performed without symmetry to confirm that all six protomers are in the PLN state (Extended Data Fig. 4e). Next, we traced back and gathered the original GJICH particles containing the hemichannel sub-particles in Class 6, and then performed 3D reconstruction with C₆ symmetry (Extended Data Fig. 4f,g). The result showed the GJICH structure with fully GCN and fully PLN hemichannels at a fairly high resolution (3.6 Å) (Fig. 3c, and Extended Data Figs. 2c,e and 4, and Table 1). It should be noted that in the GJICH particles that we used for 3D reconstruction, most PLN hemichannels would contain 1-2 GCN protomer(s) and vice versa, although these errors seemed to be mostly averaged out during image processing.

Fully GCN hemichannel in this Cx43-M257 GJICH structure was nearly identical with that in the Cx43-WT GJICH structure at pH ~8.0. The superposition of the two structures showed the average C α deviation of ~0.3 Å, indicating that this GJICH structure of Cx43-M257 is reliable (Fig. 3d, left). In contrast, fully PLN hemichannel structure was rather similar to that of the Cx46/50 GJICH structure (average C α deviation of 1.2 Å) (Extended Data Fig. 5a). For examples, W4, L7, and L10 residues of Cx43 NTH are bound to the hydrophobic surface formed by TM1 and TM2 (Extended Data Fig. 5b). Most notably, W4 residue, which is identically conserved in 18 human connexins, appeared to play a key role in stabilizing the PLN conformation by entering a deep pocket formed by two neighboring TM1s (Extended Data Fig. 5b). In addition, the loop structures between NTH and TM1 and the loosely packed unstable helix (π -helix) in the

middle of TM1 are also similar between Cx43 and Cx46/50 in PLN conformations (Extended Data Fig. 5a).

GCN-to-PLN transition accompanies dramatic structural changes of TM1 including π -helix formation.

The C α deviation between GCN and PLN hemichannels shows substantial changes in the cytoplasmic half of TMD, especially in TM1 (Fig. 3d, right) of which the middle part (residues 29–35; LFIFRIL sequence) forms an α -helix in the GCN conformation and a π -helix in the PLN conformation (Fig. 4a,b and Extended Data Fig. 5c–e). The α - to π -helix transition in TM1 necessarily causes an $\sim 55^\circ$ rotation of the cytoplasmic half, resulting in dramatic changes in the interactions of TM1 with other neighboring helices (Fig. 4c,d and Supplementary Video 1). First, F30 is dissociated from TM2 and forms new interactions with two NTHs, while R33 and F32 change side-chain conformations to maintain their original interactions (Fig. 4c,d, level 1). Second, as L29 and L26 move towards the pore, their interactions with TM4 are replaced by new interactions with TM2 and NTH (Fig. 4c,d, level 2). Third, V28, W25, and V24 of TM1, which participated in tight intermolecular interactions with TM2 of the neighboring protomer in fully GCN hemichannel, move away from TM2 and interact intramolecularly with TM4 in fully PLN hemichannel (Fig. 4c,d, level 2). This change results in a small gap between protomers, and the movement of S27 towards the gap slightly reduce the strong hydrophobicity of this region (Fig. 4d, level 2). Especially, W25, exposed to the membrane in the GCN state, moves into the hydrophilic center of TMD, participating in a hydrogen bonding with S22 and a cation- π interaction with K162 (Fig. 4c,d, level 2). When we superposed GCN and PLN hemichannels, W25 partially overlaps with the map density presumed to be CHS. Therefore, the movement of W25 during the GCN-PLN transition would slightly push the lipid out of the pocket. Fourth, in the GCN state, L11 and Q15 of NTH respectively interact with F97 and Y98 of TM2 in a neighboring protomer, and V24 of TM1 also interacts with Y98 (Fig. 4c, level 3). F97 and L11 closely contact the map density presumed to be a detergent/lipid molecule. However, in the PLN state, these interactions are broken away and the unidentified map density disappears, and an opening towards the membrane is created between protomers (Fig. 4d, level 3).

The dynamic π -helix in TM1 is one of three most conserved regions in human connexins (Extended Data Fig. 5f) and almost identically conserved in classes A and B (Extended Data Fig. 5g). In addition, V24, W25 and S27 are also quite well conserved in human connexins (Extended Data Fig. 5g). Therefore, other connexins may undergo the same structural changes of TM1 to not only regulate the intercellular transport but also create the membrane opening.

It should be noted that the W4-binding pocket is located on the extracellular half of TMD and does not change significantly during the GCN-to-PLN transition. In addition, TM1 has another π -helix at the extracellular end, which is conserved in Cx26 and Cx46/50 GJIC structures (Extended Data Fig. 5a). However, this π -helix does not undergo structural changes during the GCN-to-PLN transition (Fig. 3e).

Conformational changes in the NTH-TM1 loop and TM2-4 during the GCN-to-PLN transition.

In the GCN-to-PLN transition, substantial structural changes were observed not only in TM1 but also in other TM helices. Cytosolic halves of TM2, 3, and 4 slightly rotate around TM1 (Extended Data Fig. 6a). In addition, the loop connecting NTH and TM1 (residues 15–20) moves ~ 3 Å towards the pore inside, and the interactions of some residues in the loop (Y17, S18, and T19) with TM helices largely change (Extended Data Fig. 6b,c and Supplementary Video 2). The hydrophobic interaction of Y17 with L151, L152, and Y155 in TM3 changes to that with Y92 and V96 in TM2. The hydrogen bonding of S18 with E227 in TM4, and the hydrophobic interaction of T19 with Y230 of TM4 are broken. Only the hydrogen bonding of T19 with E227 of TM4 is remained between the loop and TM4. Therefore, during the GCN-to-PLN transition, the main interaction of the NTH-TM1 loop with TM helices changes from a stronger interaction with TM3/TM4 to a weaker interaction with TM2 (Extended Data Fig. 6e).

MD simulations identify the penetration of phospholipids through the membrane opening.

A series of structural changes in the TM helices in the GCN-to-PLN transition, including $\sim 55^\circ$ rotation and $\sim 10^\circ$ bending of TM1 by π -helix formation, results in the formation of V-shaped membrane openings between neighboring TMDs in Cx43 GJICs (Fig. 4e, and Extended Data Fig. 6d and 6F–I, and Supplementary Video 3). The surface of this intermolecular opening is formed mostly by hydrophobic and basic residues (Fig. 4f). Remarkably, the cytoplasmic halves of TM helices appear to be relatively more flexible in fully PLN hemichannel compared with fully GCN hemichannel (Fig. 4g). These structural analyses suggest that the membrane opening could be larger so that phospholipids in the inner leaflet could pass through the interprotomer gap.

To validate whether lipids can move through the membrane opening in the PLN hemichannel, we performed MD simulations based on the CHARMM36m force field⁴⁷ with corrections for charge-charge interactions^{48,49}. Because our structural models of Cx43 GJICs are missing the unstructured CLs (residues 111 to 147), we reconstructed the loops in a random configuration with no clash and no intertwining between chains. Then, we incorporated the channel into a double bilayer system of a 1-palmitoyl-2-oleoyl-*sn*-glycero-3-phosphatidylcholine (POPC), including an explicit ionic solution at 150 mM NaCl (Methods). We simulated each of the assembled systems for 400 ns in total (200 ns without any external bias followed by 200 ns at a voltage bias of 200 mV). We could detect head groups of several phospholipid molecules spontaneously inserted into the membrane opening in fully PLN GJIC, but not in fully GCN GJIC (Fig. 4h,i and Supplementary Videos 4 and 5), suggesting that phospholipid molecules may diffuse into fully PLN GJIC in a headfirst fashion. Some basic residues (K23, K109, and K234) as well as hydrophobic residues on the surface of the membrane opening are highly conserved in human connexins, suggesting that the lateral lipid transport mechanism may be similar in other connexins.

The 4:2, 3:3, and 2:4 ratios of GCN and PLN protomers in a hemichannel result in a solvent-accessible pore diameter of >14 Å.

The constriction diameter in the pore pathway of fully PLN hemichannel was ~ 10 Å. Although it is bigger than that of fully GCN hemichannel (~ 7 Å), it is not sufficiently large for efficient transport of ATP or

bigger molecules. However, we could easily predict that a hemichannel with 2 or 3 consecutive PLN protomers would have a bigger pore diameter based on our Cx43 GJIC structures. Although we could not determine the Cx43 hemichannel structures with mixed PLN and GCN protomers, we could reliably build artificial models of those hemichannels because of almost no structural difference in ECLs and the extracellular halves of TMDs between GCN and PLN protomers (Fig. 3e). We produced five hemichannel models: one with only one PLN protomer, three containing 2-4 consecutive PLN protomers, and one with five PLN protomers (Fig. 5a). In these models, we confirmed almost no steric hinderance at the interface of GCN and PLN protomers (Extended Data Fig. 6j,k).

Next, we analyzed the solvent-accessible pore diameters of the five hemichannel models and compared with those of fully GCN and PLN hemichannels (Fig. 5b). We found that the constriction diameters of the hemichannel pores formed by 4:2, 3:3, and 2:4 ratios of GCN and PLN protomers are 15.1, 16, and 14.6 Å, respectively, which are larger than the hydrodynamic diameter of ATP (~ 9.8 Å)⁴⁵.

Dynamic conformational transition of TM1 is required for the transport of large molecules.

To see whether dynamic structural transitions between GCN and PLN conformations are physiologically important for the transport of large molecules through Cx43 GJICs, we performed intercellular dye transfer experiments⁵⁰. We transfected HEK293E cells with an expression plasmid harboring the CFP-fused Cx43-WT gene, confirmed frequent formation of Cx43 gap junction, and performed scrape-loading experiments using sulforhodamine B (~ 560 Da) fluorescent dye. Next, we measured the maximum distances of dye transfer from a scrape line for 15 minutes and found that the distance in Cx43 expressing cells was three times longer than that in the control cells transfected with mock plasmid (Fig. 5e and Extended Data Fig. 7b,c).

Next, we carefully selected mutations that could destabilize the GCN state but not the PLN state (L91A and V24R) and those with the opposite effect on the two states (I31A and W25R) (Fig. 5d). The side chain of L91 in TM2 is completely exposed to the membrane in the PLN state, while this residue participates in tight intermolecular interactions with V24, W25, and V28 of TM1 in the GCN state (Fig. 5c, top panels). Therefore, the L91A mutation is likely to inhibit conformational change and increase the PLN/GCN ratio in GJICs. Conversely, the side chain of I31 in TM1 is completely exposed to the pore inside in the GCN state, while this residue engages in tight intermolecular interactions with L7, L10, V87, and I83 in the PLN state (Fig. 5c, bottom panels). Therefore, I31A is expected to lower the PLN/GCN ratio. For every scrape-loading experiment for these Cx43 mutants, we confirmed that their expression levels and gap junction formation rates were comparable with those of wild-type Cx43 (Extended Data Fig. 7b). The results showed that both mutations almost completely inhibited the dye transport activity (Fig. 5e and Extended Data Fig. 7c), suggesting that a dynamic conformational transition of TM1 is required for the transport of large molecules (Extended Data Fig. 7d and Supplementary Video 6).

In addition, mutations in V24 and W25 located near the head groups of membrane lipids were also expected to increase and decrease the PLN/GCN ratio, respectively, and thus we tested the effects of

V24R and W25R mutations on the dye transport activity (Extended Data Fig. 7a). However, although these mutations completely blocked dye transfer, they also substantially lowered the gap junction formation efficiency (Fig. 5e and Extended Data Fig. 7b,c). These mutations may also inhibit localization of Cx43 to the plasma membrane.

GCN-to-PLN transition switches electrostatic surface potential of the cytoplasmic gate from positive to negative.

Whereas the cytoplasmic surface of fully GCN hemichannel has an overall positive charge, that of fully PLN hemichannel shows a locally negative surface at the pore pathway (Fig. 6a). This change, which should affect ion transport efficiency and selectivity, is because the NTH not only bends but also rotates during the GCN-to-PLN transition, and therefore basic residues (K9 and K13) exposed on the cytoplasmic surface in the GCN conformation are partially buried at the interface between the NTHs in the PLN conformation, and acidic residues (D3 and D12) are exposed on the cytoplasmic surface of the funnel-like pore (Fig. 6b). D3 forms the pore constriction sites in both PLN and GCN conformation (Figs. 4a and 6b). D12 is involved in close intermolecular interaction(s) with R101 and K105 in the GCN conformation and with K9 in the PLN conformation (Fig. 6b). In addition, ODDD-related mutations of these two acidic residues, D3N and D12S, have been reported to reduce gap junctional conductance and lower V_j gating sensitivity, respectively^{32,34,51}.

MD simulations show anion selectivity of fully GCN GJCh and cation selectivity of fully PLN GJCh.

To investigate the ion transport mechanism through Cx43 channels, we analyzed the position-dependent local concentration and current of ionic species in MD simulations of fully PLN, 3:3 mixed (3 consecutive PLNs and GCNs) and fully GCN GJChs at a 200-mV transmembrane potential⁵²; see the gray heatmap for the local concentration and streamlines for the current (Extended Data Fig. 8a,b). We found that GCNs form a Cl^- reservoir at the entrance of the channel ($z \sim 7$ nm) with a local Cl^- concentration at the Cl^- entrance of GCN channel (>2 M) much higher than that of PLN channel (Extended Data Fig. 8b, left and right panels). Possibly due to the difference in Cl^- accumulation at the entrance, the Cl^- current through fully GCN GJCh (45 pA) was much higher than that through fully PLN GJCh (2 pA) (Fig. 6c). However, Na^+ ions are accumulated not in the Na^+ -entering hemichannel but in the Na^+ -leaving hemichannel of fully GCN GJCh (Extended Data Fig. 8a, left), suggesting that six GCNs block Na^+ ions, resulting in a Cl^- selectivity. In fully PLN GJCh, we could not observe significant accumulation of Na^+ ions, resulting in the Na^+ current (13 pA) higher than the Cl^- current (i.e., selective to Na^+) (Fig. 6c and Extended Data Fig. 8a,b, right).

We also examined the ion transport through our Cx43-WT GJCh structure with lipids that bind to the pore inside and block twelve holes between NTHs and TM2 in the GCN state. The result showed a sharp decrease of the Cl^- current, suggesting that lipids would play a major role in channel closing by blocking the six holes at the cytoplasmic gate (Fig. 6c and Extended Data Fig. 8c–e). In contrast, high Cl^- selectivity remained regardless of bound lipids (Fig. 6c and Extended Data Fig. 8c–e), supporting our

conclusion that fully GCN GJICH is Cl⁻-selective and fully PLN GJICH is Na⁺-selective. In addition, only slight increase in the ionic current and no charge selectivity in the 3:3 mixed hemichannel suggests that electrostatics would be more important in ion transport than the pore size (Fig. 6c and Extended Data Fig. 8a,b, middle). It should be noted that Cl⁻-transport activity and selectivity of fully GCN GJICH may not be physiologically relevant, because the pore in the state may contain more lipids, which were not included in our simulations.

Cx43-WT GJICH at pH ~6.9 has protomers in the PLN conformation.

Since Cx43-WT GJICH exhibits the maximum H⁺ ion transmission at pH 6.9 and the minimum at pH 6.4 or lower⁴⁰, we aimed to unravel the structures at pH 6.9 and pH 6.4. For the cryo-EM imaging, we lowered the pH of the protein sample from ~8.0 to ~6.9 and ~6.4 just before vitrification. While Cx43-WT GJICHs at pH ~6.4 were severely denatured and aggregated, those at pH ~6.9 were relatively stable (Fig. 7a) and their structures determined with D6 symmetry to 3.4 Å resolution. We then performed the same protomer-based conformational variation analysis as in the study of Cx43-M257 GJICHs (Fig. 7b and Methods). We could find a protomer class (Class 2; 7.8%) with the PLN conformation in single-subunit-focused 3D classification. The investigation of the original GJICH particles to which PLN protomers in class 2 belonged showed that ~44% GJICH particles were in the fully GCN state, ~33% contained one PLN protomer, and ~20% contained two or three PLN protomers (Fig. 7c). These data suggest that pH ~6.9 increases the structural flexibility of Cx43 to cause various GCN and PLN protomer compositions in GJICHs, although the effect of pH ~6.9 is lower than that of CTL deletion (Figs. 3b and 7c).

Structural stabilization of the CL in the PLN state.

In the Cx43-M257 GJICH structure, we found a strong map density corresponding to the CL in fully PLN hemichannel, but not in fully GCN hemichannel (Fig. 7d,e). Although this map was not sufficiently clear to correctly register the residues of the CL, we could conclude that it includes the total length of the CL (residues 111–147) based on the length of continuous map and the connectivity with TM2 and TM3. This stabilization of the CL could also be detected in PLN protomers in the dataset of Cx43-WT at pH ~6.9 (Fig. 7b). The CL map is in a large-area contact with the cytoplasmic protrusion of TM2 and the NTH-TM1 loop (Fig. 7e,f), suggesting that this interaction could stabilize the PLN conformation. The contact sites include a hydrophobic patch formed by Y17 of the NTH-TM1 loop, Y92 of TM2, and Y155 of TM3, which may interact with hydrophobic residues in the CL (Fig. 7e,f).

Discussion

We determined the structures of Cx43 in two different conformations (GCN and PLN) and revealed that the GCN-to-PLN transition includes not only the conformational change of NTH but also π -helix formation in the middle of TM1 and reorganization of the interaction network among all TM helices. Although high resolution structures were solved in a detergent environment, we confirmed the GCN conformation from a lower resolution structure in lipid nanodiscs (Fig. 1e and Extended Data Fig. 1e), and the available

Cx46/50 structure in lipid nanodiscs showed a very similar PLN conformation (Extended Data Fig. 4a). Based on these structures, we could also design several point mutations that would inhibit conformational transition without disturbing structural integrity. Our dye transfer study in human cells confirmed that those mutations indeed abolish the transport activity through Cx43 GJICs (Fig. 5e). These data strongly support the physiological relevance of two identified Cx43 conformations.

We took advantage of cryo-EM technology that can identify conformational variants, and found that purified Cx43 GJICs in channel opening conditions (pH ~6.9 or deletion of C-terminal 125 residues) contain various compositions of GCN and PLN protomers in a single channel (GCN:PLN from 11:1 to 0:12). This led us to rethink the open state of this channel and hypothesize that a hemichannel with 2:4, 3:3, or 4:2 of GCN:PLN protomers may represent the fully open state. The pore diameters of <math><12 \text{ \AA}</math> observed in available connexin and pannexin channel structures have raised a question of how big molecules such as ATP or NADH could pass through this small pore⁵³. In addition, it has been a mystery how Cx43 GJIC has at least three conductance states (closed, open, and residual states) observed in numerous electrophysiology experiments. About 7 to 16 Å pore sizes created by various compositions of GCN and PLN protomers in a GJIC may help answer these questions.

It should be noted that the distribution of PLN/GCN ratios in Cx43 GJICs described in this study, especially that at pH ~6.9, may not represent those in their physiological membrane environment. Although we confirmed that Cx43 at pH ~8.0 is mainly in the GCN state in both lipid and detergent environments, conformational preference of Cx43 may at least be partially dependent on its lipid environment. In addition, many factors in the cell membrane and cytoplasm could change the PLN/GCN ratio distribution of individual GJICs in gap junction plaques.

We showed that basic pH induces the channel closing by decreasing the PLN/GCN ratio in hemichannel. Basic pH is thought to be sensed by C298 residue at CTL⁴⁰. Since the CL is located between NTH and CTL, some changes in CTL would be transferred to NTH not directly but via the CL. Therefore, it was hypothesized that CTL, which is dissociated from the CL at neutral pH, would be bound to the CL at basic pH resulting in the channel closing. This idea is supported by the strong map density of the CL bound to TM2 and the NTH-TM1 linker in the PLN conformation (Fig. 7e). Since the map density of the CL is not seen in the GCN conformation, we think that the CL is released from TM2 and the linker at a basic pH by the interaction with CTL, and thus the GCN conformation become more favorable. Similar to the mechanism of how pH regulates the gating, other regulatory factors may also not target NTH directly but other regions to eventually induce conformational change of NTH via that of TM1 or the CL.

The sequence analysis of the connexin family (Extended Data Fig. 5g) suggests that some of the structural changes shown in Cx43, such as π -helix formation in the middle of TM1 and the interaction of N-terminal tryptophan with the hydrophobic pocket formed by two TM1s and TM2, may be conserved in other connexin family members. However, the hydrophobic residues involved in the intramolecular interaction between NTH and TM2, which is crucial for the GCN conformation, are conserved only in A and C class connexins (Fig. 2c). Therefore, connexins in other classes may have a different NTH

conformation when it is dissociated from TMD. This is consistent with the structures of Cx26 in B class, which showed α -helix in the middle of TM1 but flexible NTHs^{5,6}. None of Cx26 GJICH structures showed π -helix in the middle of TM1 and W3 (corresponding to W4 in Cx43) bound to the hydrophobic pocket formed by two TM1s, although the π -helix-forming residues, W3, and the pocket-forming residues are highly conserved in this channel. Cx26 may have the PLN conformation similar as shown in Cx43 for a short time or in an unknown condition.

Cx46 and Cx50 preferably adopt the PLN conformation in both detergent and lipid environments. These members may function only as fully PLN GJICH with the mission of ion transfer. Alternatively, they may be able to transport large molecules by PLN-to-GCN transition of 2-4 consecutive protomers in a hemichannel. Since the residues involved in the intramolecular interaction of NTH and TM2 in the Cx43 GCN conformation are highly conserved in Cx46 and Cx50, Cx46/50 likely undergoes the same conformational change as Cx43.

The pore inside in the fully GCN state has lipid molecules tightly bound to the hydrophobic surface, whereas that in the fully PLN state has hydrophilic surface without bound lipids (Figs. 2a and 6a, left and right). Therefore, lipids in the pore in the GCN state should be exported to the membrane during the conformational transition for gating regulation. We found the membrane opening between PLN protomers similarly as observed in innexin-6 GJICH structure in lipid nanodiscs⁵⁴, and our MD simulation study showed lipid molecules can pass through the membrane openings of fully PLN GJICH (Fig. 4i). These data suggest that the dynamic conformational changes of individual protomers in Cx43 GJICH facilitate not only the intercellular transport of ions/metabolites through but also the lateral lipid transport in and out of the channel pore.

Methods

Plasmid construction and mutagenesis.

A synthetic gene fragment encoding the full-length human Cx43 (*GJA1*) (UniProt ID # P17302) was purchased from Integrated DNA Technologies and inserted into pX vector as previously reported⁵⁵. The human Cx43-WT proteins were expressed as fusion constructs with a human rhinovirus (HRV) 3C cleavage site, an enhanced yellow fluorescence protein (eYFP) tag, a 10'His-tag and a rho-1D4 epitope tag (8 amino acid sequence of TETSQVAPA) at its C-terminus. To make a Cx43-M257 expression plasmid, the PCR-amplified gene fragment encoding 1-257 amino acids of human Cx43 was inserted in pX vector. For dye transfer assay, we also produced the expression plasmid containing an enhanced cyan fluorescence protein (eCFP)-fused version of Cx43-WT to avoid the interference with a fluorescent signal from sulforhodamine B (SRB) dye. Using this plasmid as a template, we introduced point mutations by PCR to make the expression plasmids of Cx43 mutants.

Protein expression and purification of human Cx43-WT.

Cx43-WT expression plasmids were amplified in *Escherichia coli* DH5α strains, purified, mixed with linear polyethylenimine (PEI, Polysciences, Inc.), and transfected into human embryonic kidney 293E (HEK293E) cells^{55,56}. When the HEK293E suspension cells (2 L) were grown at 37°C to a density of $\sim 0.6 \times 10^6$ cells/ml in Ca²⁺-free Dulbecco's modified Eagle's medium (DMEM) supplemented with 5% fetal bovine serum, the mixtures of DNA and PEI were added to the cells. Dimethyl sulfoxide (Amresco) was added to the final concentration of 1%, and temperature was lowered to 33°C immediately after transfection. Tryptone (Amresco) was added 48 hours after transfection to the final concentration of 0.5%. The transfected cells were harvested 96 hours after transfection.

All purification steps were carried out at 4°C unless indicated otherwise. The harvested cells were resuspended in buffer A [20 mM CAPS (pH 10.5), 250 mM KCl, and 2 mM β-mercaptoethanol] supplemented with 10% glycerol, 2 μg/ml *Staphylococcus aureus* nuclease (SA nuclease), 5 mM CaCl₂, 1 mM phenylmethylsulfonyl fluoride (PMSF), and one tablet of EDTA-free Pierce protease inhibitor tablets (Thermo Fisher Scientific, catalog no. 88666). The resuspended cells were lysed using a Dounce homogenizer (Bellco) with a tight (B) pestle (25–30 strokes), and the membrane fraction was isolated by high-speed centrifugation at 42,600g for 1 hour. The membrane pellets were resuspended using a WiseTis homogenizer (Daihan Scientific Co., Ltd.) in 50 ml buffer A supplemented with 2% glycerol, 1 mM PMSF, 2 mM EDTA, 2 mM EGTA, one tablet of EDTA-free Pierce protease inhibitor tablets, and 0.5/0.05% (w/v) LMNG/CHS (Anatrace, catalog no. NG310-CH210). After incubation for 1 hour with slow rotation, the samples were mixed with 2.5 ml of neutralization buffer containing 1 M Tris (pH 7.5) to lower the pH of samples to ~ 8.0 and centrifuged at 42,600g for 1 hour. The supernatant was mixed with adipic acid dihydrazide-agarose resin (Sigma, catalog no. A0802) conjugated with rho-1D4 antibody (University of British Columbia) in an open column (Bio-Rad) and incubated for 1 hour with gentle rotation. The resins were settled down in the column and washed twice with 10 column volumes (CVs) of buffer B [20 mM Tris (pH 8.0), 250 mM KCl, 2 mM β-mercaptoethanol, 2% glycerol, and 0.004/0.0004% (w/v) LMNG/CHS], and once with 10 CVs of buffer C [20 mM Tris (pH 8.0), 250 mM KCl, 2 mM β-mercaptoethanol, and 0.004/0.0004% (w/v) LMNG/CHS]. The bound proteins were incubated for 2 hours with the addition of excess HRV 3C protease (~ 0.25 mg) to cleave off the C-terminal eYFP-rho-1D4 tag from Cx43-WT proteins, and eluted from the resin. To remove possible post-translational modifications (PTMs) on Cx43, the eluted proteins were incubated for 2 hours with lambda protein phosphatase (λ-PPase) and universal deubiquitinase DUB (M48) at a 15:1 (w/w) ratio of Cx43 to the enzymes. For the activation of λ-PPase, 1 mM MnCl₂ was added to the reaction buffer, and the reaction was stopped by adding 5 mM EDTA after 2 hours. Next, the proteins were concentrated to ~ 3 mg/ml using an Amicon Ultra centrifugal filter (molecular weight cutoff, 100 kDa), filtered with a 0.22 μm filter, and then loaded on a *Superose 6 Increase 10/300 column* (GE Healthcare) equilibrated with buffer C. Peak fractions were pooled, concentrated to ~ 3.2 mg/ml, flash-frozen in liquid nitrogen, and stored at -80°C for nanodisc reconstitution and EM grid preparation. Protein purity and quality were assessed by SDS-polyacrylamide gel electrophoresis (SDS-PAGE) and negative-stain EM.

Protein expression and purification of Cx43-M257.

Cx43-M257 was expressed in HEK293E cells in the same method as in the Cx43-WT expression. Protein purification was carried out at 4°C. The transfected cells were lysed using a Dounce homogenizer in buffer D [20 mM Tris (pH 8.0), 250 mM NaCl, 10% glycerol, 0.1 mM PMSF, one tablet of EDTA-free Pierce protease inhibitor tablets, RNase A, and SA nuclease]. The lysate was centrifuged at 35,000g for 1 hour, and the pellets were washed in buffer E [20 mM (pH 8.0), 1 M NaCl, 1 mM EDTA, 2% glycerol, and protease inhibitor cocktail]. Membrane proteins were extracted in buffer F [20 mM CAPS (pH 10.5), 150 mM KCl, 2% glycerol, 2 mM β -mercaptoethanol, 1 mM EDTA, 0.5/0.05% (w/v) LMNG/CHS, and protease inhibitor cocktail] for 1 hour with gentle rotation and then centrifuged at 20,000g for 1 hour. The supernatant was mixed with agarose resin conjugated with rho-1D4 antibody at 4°C for 2 hours and washed three times with 10 CVs of buffer G [20 mM Tris (pH 8.0), 150 mM KCl, and 2 mM β -mercaptoethanol] supplemented with 2% glycerol, and 0.005/0.0005% (w/v) LMNG/CHS. Bound proteins were eluted by adding a 1:20 (w/w) of HRV 3C protease and overnight incubation. The eluted protein was concentrated and loaded on a Superose 6 Increase 10/300 column equilibrated with buffer G supplemented with 0.005/0.0005% (w/v) LMNG/CHS. Peak fractions were pooled, concentrated to ~3 mg/ml, flash-frozen in liquid nitrogen, and stored at -80°C.

Expression and purification of membrane scaffold protein.

The membrane scaffold protein (MSP1E3D1) was expressed and purified as previously described⁵⁷, with slight modifications. The pET28a plasmid containing MSP1E3D1 gene was obtained from Addgene (plasmid #20066). *E. coli* BL21 (DE3) competent cells were transformed with pET28a-MSP1E3D1 and grown on SOC plates containing 30 μ g/mL kanamycin. A single colony was picked and cultured in terrific broth supplemented with 30 μ g/mL kanamycin at 37°C. When the cell density reached an OD₆₀₀ of 1.2~1.4, protein expression was induced by 1 mM IPTG for 3 hours at 37°C. The cells were harvested by centrifugation at 8,000g for 30 min. The cell pellet was resuspended in buffer H [20 mM Tris (pH 8.0), and 250 mM NaCl] supplemented with 10% glycerol, 1% (w/v) Triton X-100, and 1 mM PMSF. The cells were lysed by sonication and centrifuged at 40,000g for 1 hour. The supernatant was loaded onto a nickel-nitrilotriacetic acid (Ni-NTA) resin equilibrated with buffer I [20 mM Tris (pH 8.0), 250 mM NaCl, and 1% (w/v) Triton X-100]. The Ni-NTA resin was washed by the following buffers (5 CV each): buffer I, buffer I supplemented with 20 mM imidazole, buffer H supplemented with 40 mM imidazole. The bound proteins were eluted by buffer H supplemented with 300 mM imidazole. To remove imidazole, the eluted proteins were loaded onto a HiPrep 26/10 desalting column (GE Healthcare) equilibrated with buffer H. The eluted MSP1E3D1 sample was supplemented with 1 mM EDTA, concentrated to ~3.6 mg/ml, flash-frozen in liquid nitrogen, and stored at -80°C.

Reconstitution of Cx43-WT in lipid nanodiscs.

Purified Cx43-WT was reconstituted into lipid nanodiscs as previously described⁵⁷, with some modifications. Soybean polar lipid extract powder (Avanti Polar Lipids) was dissolved in chloroform, aliquoted, and dried completely to be a thin layer using argon stream. Just before reconstitution, the lipid

film was solubilized in 5/0.5% (w/v) LMNG/CHS, and incubated at 60°C for 30 min to make a clear lipid stock solution at a concentration of ~10 mg/ml.

All the reconstitution steps were carried out on ice. Cx43-WT sample (~3.2 mg/ml, 0.68 mL) was mixed with the lipid stock (~10 mg/ml, 0.26 mL) at the 1:66 molar ratio of Cx43-WT to lipid, and incubated for 20 min. Next, MSP1E3D1 (~3.6 mg/ml, 0.14 mL) was added to the Cx43-lipid mixture at ~1:0.3 molar ratio of Cx43-WT to MSP1E3D1, and incubated for 40 min. Bio-beads SM2 absorbent (120 mg per 1 ml mixture, Bio-Rad) pre-washed with buffer G were added to the Cx43-lipid-MSP mixture to remove detergents, and incubated overnight with slow rotation. Bio-beads were removed by centrifugation and fresh Bio-beads were added and incubated for 4 hours to remove residual detergents. After Bio-beads were removed, the reconstituted mixture was concentrated to reduce the sample volume up to 500 μ l, filtered with a 0.22 μ m filter, and loaded on a Superose 6 Increase 10/300 column equilibrated with buffer G. Peak fractions containing Cx43 in nanodiscs were pooled, and concentrated to ~2.2 mg/ml for EM grid preparation. The reconstitution quality was assessed by SDS-PAGE and negative-stain EM.

Cryo-EM grid preparation and data collection.

The purified Cx43 GJICH samples in detergents or in lipid nanodiscs are in buffer at pH 8.0. For the grid preparation of Cx43-WT and Cx43-M257 samples in detergents at pH 8.0, 3 μ l protein samples (1.4 mg/ml for Cx43-WT and 2.3 mg/ml for Cx43-M257) were applied onto glow-discharged (15 mA current; negative charge; 60 sec) holey carbon grids (Quantifoil R1.2/1.3 Cu 200 mesh, SPI). The grids were blotted for 6.5 sec using a Vitrobot Mark IV (Thermo Fisher Scientific, USA) at 4°C with 100% humidity and vitrified by plunging into the liquid ethane cooled by liquid nitrogen. For preparation of Cx43-WT samples in detergents at pH 6.9, a buffer containing 500 mM HEPES (pH 6.8), 150 mM KCl, 2 mM β -mercaptoethanol, and 0.004/0.0004% (w/v) LMNG/CHS was added to the Cx43-WT samples in detergents at pH 8.0 at a ratio of 1:3 (v/v), just before vitrification. After three microliters of protein samples (0.7 mg/ml) were loaded onto holey carbon grids (Quantifoil R1.2/1.3 Cu 200 mesh), the grids were blotted and vitrified in Vitrobot. The conditions of glow-discharging and blotting were same as mentioned above. For the grid preparation of Cx43-WT samples in nanodiscs at pH 8.0, glycerol was added to the protein samples at a final concentration of 1% (v/v) to make protein particles disperse evenly. Three microliters of protein samples (1.7 mg/ml) were applied onto glow-discharged (15 mA current; positive charge; 60 sec) holey carbon grids (Quantifoil R1.2/1.3 Cu 200 mesh). The grids were blotted for 7.0 sec and vitrified in Vitrobot.

Cryo-EM data were collected at Korea Basic Science Institute (Ochang, Korea) using a Titan Krios (Thermo Fisher Scientific, USA) transmission electron microscope operated at 300 kV. Movie data were recorded using Falcon 3EC direct electron detector (Thermo Fisher Scientific, USA) with electron counting mode and automatic data acquisition software (EPU; Thermo Fisher Scientific, USA). Three datasets of Cx43 samples in the presence of detergents (Cx43-WT at pH 8.0 and pH 6.9, and Cx43-M257 at pH 8.0) and a dataset of Cx43-WT in nanodiscs at pH 8.0 were recorded with a calibrated pixel size of 0.675 Å and 0.5235 Å, respectively. Detailed data acquisition conditions and parameters are provided in Table 1.

Cryo-EM data processing.

All datasets of Cx43 samples were processed with RELION 3.1⁵⁸ or cryoSPARC version 3.1⁵⁹ softwares. The overall workflow for data processing is presented in Extended Data Figs. 1 and 4. For the dataset of Cx43-WT in detergent solution at pH 8.0, RELION 3.1 was used for the processing. Beam-induced motion correction and dose weighting of raw movies were performed using MotionCor2 version 1.2.6⁶⁰. Contrast transfer function (CTF) estimation was performed using Gctf version 1.18⁶¹. Micrographs unsuitable for further image processing such as those containing ice crystals, large motion drifts, extremely low or high defocus, and large astigmatisms were removed by manual inspection and selection job in RELION. As a result, 4,344 micrographs were selected for further processing, and then 1,130,417 semiautomatically picked particles were extracted into 400 × 400 pixel boxes. Many false-positive images, poorly aligned particles, off-centered particles, and undocked hemichannel particles were discarded by performing 12 rounds of two-dimensional (2D) classification. Using 293,152 sorted particles, a 3D initial model of Cx43 GJICH was generated by a stochastic gradient descent algorithm in RELION with C1 symmetry. After 4 rounds of 3D classification with C1 or D6 symmetry imposition, 26,451 selected particles in the classes with good quality side views of GJICHs were used in 3D refinement. Per-particle motion drifts of assorted particles were corrected using Bayesian polishing⁶² and 3D refinement with D6 symmetry imposition was performed, generating a 3.4 Å map. After one more round of 3D classification without orientation search, 21,689 selected particles were subjected to 3D refinement with D6 symmetry imposition, resulting in a 3.3 Å map. For further improvement of the map, per-particle CTF estimation was performed using CTF refinement⁶³ in RELION. After 3D refinement with D6 symmetry imposition, the estimated resolution of the final map was 3.1 Å based on the 0.143 Fourier shell correlation (FSC) criterion⁶⁴. The local resolution of the density map was assessed by ResMap⁶⁵.

For the dataset of Cx43-WT in nanodiscs at pH 8.0, cryoSPARC was used for the processing. Beam-induced motion correction and dose weighting of raw movies were performed using patch motion correction. Then, CTF parameters were estimated using patch CTF estimation for further CTF correction. 1,683,178 particles were picked from 6,760 micrographs using Template picker with the initial 2D templates, which were generated by randomly selected 500 micrographs using Blob picker, and extracted into 512 × 512 pixel boxes. After first 2D classification, only 52,110 particles were selected due to the extremely high false-positive rates and the large numbers of atypical particles. In addition, the number of side-view particles were insufficient to make a reliable 3D reconstruction map. To increase the number of side-view particles, we used Topaz⁶⁶ in cryoSPARC for particle picking, resulting in 73,964 side-view particles. Top-view particles previously selected by Template picker and side-view particles selected by Topaz were combined for the further steps. Finally, 28,341 particles with various orientations were selected by two more rounds of 2D classification and used for local motion correction and 3D homogenous refinement with D6 symmetry imposition. The estimated resolution of the final map was 3.6 Å based on the 0.143 FSC criterion. The local resolution of the density map was assessed by ResMap.

For the dataset of Cx43-M257 in detergents at pH 8.0, RELION 3.1 was used through the processing. Motion correction and CTF estimation were performed using the MotionCorr2 and the Gctf, respectively. After removal of micrographs unsuitable for image processing, 2,781 micrographs were selected, and 559,754 semiautomatically picked particles were extracted into 400 × 400 pixel boxes. After 5 rounds of 2D classification, several rounds of 3D classification were performed with C1 or D6 symmetry. In the first 3D classification, the final map of Cx43-WT GJICH in detergents at pH 8.0 was low-pass-filtered to 30 Å and used as a reference map. Selected 59,789 particles classified into different classes with good quality side views of GJICHs were subjected to 3D refinement. After Bayesian polishing, 3D refinement with D6 symmetry imposition were performed to generate 3.3 Å map.

The dataset of Cx43-WT in detergents at pH 6.9 was processed in the same protocol. Motion correction and CTF estimation were performed using the MotionCorr2 and the Gctf, respectively. After removal of micrographs unsuitable for image processing, 2,997 micrographs were selected, and 3,224,367 semiautomatically picked particles were extracted into 400 × 400 pixel boxes. After 16 rounds of 2D classification, several rounds of 3D classification were performed with C1 or D6 symmetry imposition. In the first 3D classification, the final map of Cx43-WT GJICH in detergents at pH 8.0 was low-pass-filtered to 30 Å and used as a reference map. Selected 8,861 particles classified into different classes with good quality side views of GJICHs were subjected to 3D refinement. After Bayesian polishing, 3D refinement with D6 symmetry imposition were performed to generate 3.5 Å map.

Focused classification on protomers and determination of the number of PLN protomers in GJICH.

In the datasets of both Cx43-M257 in detergents at pH 8.0 and Cx43-WT in detergents at pH 6.9, during 3D classification steps with C1 symmetry, we identified two noticeable classes with and without NTH densities. To distinguish possible different classes representing various conformations of NTHs, we used single protomer-based conformational variation analysis⁶⁷. For this analysis, 3.3 Å map of Cx43-M257 in detergents at pH 8.0 and 3.5 Å map of Cx43-WT in detergents at pH 6.9 were used as consensus maps. Using already well-aligned particles used for reconstructing the consensus maps, we ran a command “relion_particle_symmetry_expand” in RELION 3.1 to produce 11 copies of each particle by computationally rotating and tilting based on the D6 symmetry axis. This resulted in 12 times the total number of particles, which were subjected to Particle subtraction job to generate subtracted particles containing only the signal of one protomer. The subtracted particles were re-centered and re-extracted into 200 × 200 pixel boxes, and subjected to a focused 3D classification (K=8; the number of classes to classify is 8) with a mask covering one protomer and without orientation search. This resulted in two distinct classes of protomers with GCN and PLN conformations for both Cx43-M257 (pH 8.0) and Cx43-WT (pH 6.9) datasets (Figs. 3a and 7b).

To see the distribution of how many PLN protomers (protomers in the PLN conformation) are included in each GJICH particle, we analyzed the metadata files generated by focused 3D classification. The metadata contains all subtracted protomer particles labeled with the class number of each protomer and the identification (ID) number of each original GJICH particle. Because of D6 symmetry expansion, the

same identification number of GJICH should be found 12 times in the metadata. The metadata was sorted by the protomer class numbers from focused 3D classification, and the GJICH ID numbers were collected only for the classes with the PLN conformation. How many times the same ID is repeated in the collection indicates how many PLN protomers are included in the corresponding GJICH particle. To sort particles in the metadata, count the number of repetitions of a GJICH ID, and calculate the number of GJICHs with each of 13 different protomer compositions (0:12 to 12:0 of GCN and PLN) at the same time, we used a shell command below.

```
cat XXX_data.star | grep @ | awk '{if($3==X||$3==Y) print $27}' | uniq -c | sort | awk '{print $1}' | uniq -c
```

In this command, “grep @” is for printing without the information of optic group and metadata labels, and “awk '{if(\$3==X||\$3==Y) print \$27}'” is for printing only 'ImageOriginalName' belonging to X or Y class (i.e., protomer classes in the PLN conformation).

Structure determination of fully PLN hemichannel by focused classification and localized reconstruction.

The Cx43-M257 dataset and its 3.3 Å consensus map were used for focused classification on and localized reconstruction of hemichannels. We followed the procedures reported by Gestaut et al⁶⁸. The overall workflow is presented in Extended Data Fig. 4. We used two masks covering each hemichannel of the consensus GJICH map to generate the subtracted particles in two opposite orientations. After re-centering and re-extraction into 300 × 300 pixel boxes, we subjected the subtracted particles to 3D classification (K=6) with C1 symmetry imposition to align into one orientation. We chose five hemichannel classes (Class 1, 3, 4, 5, and 6) with good quality side views and performed focused 3D refinement (C1 symmetry) with a soft mask covering hemichannel to obtain a hemichannel map at 3.8 Å resolution. Using this map as a new consensus map, we ran 25 iterations of 3D classification (K=8, T=4; T is Regularisation parameter) without orientation search. The result showed three hemichannel classes (Class 2, 5, and 6) containing one or two PLN protomer(s). In additional 15 iterations of 3D classification, we increased the T value (T=40) and applied a soft mask covering the cytoplasmic half of hemichannel to focus more on the conformational changes of NTHs. This generated one unique class (Class 6) in the fully PLN state. 8,046 particles in Class 6 were subjected to 3D refinement with C1 symmetry imposition and 1.8° angular sampling, which produced a 7 Å map. Another round of focused 3D refinement with C6 symmetry imposition resulted in a 4.3 Å map. Next, we traced back the original GJICH particles from which the subtracted hemichannel particles came, and redundant particles were removed. Without changing particle's orientations from focused 3D refinement, total 7,446 GJICH particles were subjected to 3D refinement with C6 symmetry imposition and 1.8° angular sampling. The result showed a 3.6 Å GJICH map with fully PLN hemichannel on one side and fully GCN hemichannel on the other side. This map was not subjected to sharpening because it significantly weakens map densities of NTHs. The local resolution of the density map was assessed by ResMap.

Model building, validation, and structural analysis.

The structural model for the Cx43-WT GJIC in detergents at pH 8.0 was built manually in Coot program^{69,70} and refined using phenix.real_space_refine⁷¹ in PHENIX software suite with secondary structure and non-crystallographic symmetry (NCS) restraints. This structure does not contain Met1 and N-terminal acetylation (see the main text for details). The final model also does not include flexible cytoplasmic regions such as CLs (residues 111-147) and CTLs (residues 236-382) because the map densities of these regions are invisible. We also put acyl chain models into long map densities around TMDs, but did not put any lipid model into unidentified densities presumed to be a head group of phospholipids/detergents and a sterol because of ambiguous map densities. The geometric restraints for acyl chains were optimized using the eLBOW module⁷² in PHENIX. For the model of Cx43-WT GJIC in nanodiscs at pH 8.0, the protein model in detergents at pH 8.0 was fitted into the map density using Chimera's Fit in Map tool, and real-space refinement were performed in PHENIX with secondary structure and NCS restraints.

For the structure of Cx43-M257 GJIC (C6 symmetry) composed of a PLN and a GCN hemichannel, we first performed homology modelling in the *SWISS-MODEL* server⁷³ using an available Cx46 structure (PDB code number 7JKC)⁷⁴ as a template. The predicted Cx43 model was fitted into one PLN protomer map of the Cx43-M257 GJIC map in Chimera, manually modified in Coot, and refined in PHENIX. The refined model of one protomer in the PLN conformation was fitted into the five other PLN protomer maps. For modelling the GCN hemichannel part, a hemichannel model from the Cx43-WT GJIC structure in detergents at pH 8.0 was fitted into the map in Chimera, and then the dodecameric model was refined in PHENIX (real-space refinement) with secondary structure and NCS restraints.

For validation of structural models, FSC curves were calculated between EM maps and final models. The qualities of final models were evaluated using MolProbity⁷⁵ in PHENIX. Detailed statistics for model refinement and validation are presented in Table 1. The pore radii and the surface of the pore pathway were calculated using HOLE⁷⁶ and CAVER v.3.03⁷⁷. Figures were produced with Chimera and Pymol.

MD simulation protocol.

For all MD simulations, we used the GROMACS 2020.2 package⁷⁸ and the CHARMM36m force field⁷⁹, combined with the CHARMM-modified TIP3P model and the CUFIX corrections for charge-charge interaction pairs⁸⁰. All simulations were performed under a constant surface tension–constant temperature (NPgT) ensemble at zero surface tension ($g = 0$)⁸¹ and 300 K temperature⁸². Van der Waals forces were computed using a 10- to 12-Å switching scheme. Long-range electrostatic forces were computed using the particle-mesh Ewald summation scheme⁸³ of a 1.2-Å grid spacing and 12-Å real-space cutoff. Covalent bonds to hydrogen in non-water and water molecules were constrained using the LINCS⁸⁴ and algorithms⁸⁵, respectively. During MD simulations using a 2-fs time step, we saved atomic coordinates every 20 ps for analysis. The visualization scheme for the density-flux map is described in a previous report by Yoo and Aksimentiev⁸⁶.

MD preparation of Cx43 GJIC embedded in a lipid bilayer.

We manually reconstructed the unstructured CL of each Cx43 chain (residues 111 to 147) missing in experimental GJIC models; the reconstructed loops were in a random configuration with no clash and no intertwining between chains. To create a double bilayer system, we placed a lipid bilayer of a 1-palmitoyl-2-oleoyl-*sn*-glycero-3-phosphatidylcholine (POPC) near the transmembrane domain of each hemichannel and removed lipid molecules overlapping with the channel. We immersed the complex system of lipid molecules and the channel in an explicit solution of 150 mM NaCl. The final system contained a channel, 734 POPC lipids, 88,000 water molecules, 300 Na ions, and 360 Cl ions in a periodic hexagonal box (. We energy-minimized each system for 5000 steps and equilibrated it for 200 ns with the positions of experimentally determined heavy atoms harmonically constrained using a force constant of 1,000 kJ/mol; note that we did not constrain the positions of reconstructed CLs. For the measurements of ionic currents, we performed a 200-ns simulation under 200 mV without any constraints for each system, starting from the final structure of the equilibration.

Scrape-loaded dye-transfer assay.

Scrape-loaded dye-transfer assays were performed according to the method described previously^{87,88}, with some modifications. Briefly, HEK293E cells were grown to 50-60% confluency in 24-well plates and transiently transfected with Cx43-eCFP expression plasmids. The cells were rinsed twice with Hank's Balanced Salt Solution (HBSS; Sigma) and added with 0.15% sulforhodamine B (SRB) (559 Da; Sigma) in HBSS. The cells were scraped using a pipette tip and incubated at 37°C for 15 min. After washing three times with HBSS, the cells were observed with an EVOS fluorescence microscope (Thermo Fisher Scientific). To determine the extent of dye transfer, the distance of dye spread from the scrape line was measured in ImageJ software. For each of wild-type, mutant, and mock plasmids, the dye spread distances in total 9 areas were measured and averaged to produce the graph represented in Fig. 5e. In each experiment, we first turn on the blue fluorescence detection mode (Excitation (Ex)/ Emission (Em) = 360/447 nm) in the EVOS FL microscope to select an area of confluent cells with high CFP signals around a scrape line, and then turn on the red fluorescence detection mode (Ex/Em = 530/593 nm) to see SRB signals in the selected area. We took a picture of the SRB signals and measured the maximum distance of dye spread at the whole area using ImageJ program. We analyzed 3 areas for each experiment and performed three independent experiments.

Declarations

Data availability

All data needed to evaluate the conclusions in the paper are present in the paper and/or the Supplementary Information. Additional data related to this paper may be requested from the authors. The Cryo-EM density maps for Cx43-WT GJIC in detergents and nanodiscs, and Cx43-M257 GJIC in

detergents have been deposited in the EM Data Bank (<http://emdatbank.org/>) under the accession codes EMD-31495 (fully GCN GJICH), EMD-31496 (fully GCN GJICH), and EMD-31497 (GJICH with fully GCN and fully PLN hemichannels), respectively. The atomic coordinates for Cx43-WT GJICH in detergents and nanodiscs, and Cx43-M257 GJICH in detergents have been deposited in the Protein Data Bank under accession codes 7F92 (fully GCN GJICH), 7F93 (fully GCN GJICH), and 7F94 (GJICH with fully GCN and fully PLN hemichannels), respectively.

Acknowledgements

We thank Amer Alam at the University of Minnesota for critical reading of the manuscript, and Jeessoo Kim and Jong-Seo Kim at the Seoul National University for mass spectrometry experiments and data analyses. This work was supported by the Suh Kyungbae Foundation (SUHF-18010097 to J.-S.W.), the National Research Foundation (NRF) grants funded by the Ministry of Science and ICT (NRF-2018R1C1B6004447 to J.-S.W. and NRF-2020R1A2C1101424 to J.Y.), and by the National Supercomputing Center (KSC-2020-CRE-0080 to J.Y.).

Author contributions

J.-S.W. conceived this project; H.-J.L., H.J.C., S.-N.L., and C.-W.L. purified GJICHs; H.-J.L. and H.J. performed electron microscopy; H.-J.L., H.J.C., and H.J. analyzed the EM data and determined the structures; H.J.C. performed dye transfer assays; M.K. and J.Y. performed MD simulations; H.-J.L., H.J.C., H.J. and J.-S.W. wrote the manuscript.

Competing interests

The authors declare no competing interests.

References

1. Goodenough, D.A. & Paul, D.L. Gap junctions. *Cold Spring Harb Perspect Biol* **1**, a002576 (2009).
2. Unwin, P.N. & Zampighi, G. Structure of the junction between communicating cells. *Nature* **283**, 545-9 (1980).
3. Unwin, P.N. & Ennis, P.D. Two configurations of a channel-forming membrane protein. *Nature* **307**, 609-13 (1984).
4. Unger, V.M., Kumar, N.M., Gilula, N.B. & Yeager, M. Three-dimensional structure of a recombinant gap junction membrane channel. *Science* **283**, 1176-80 (1999).
5. Maeda, S. et al. Structure of the connexin 26 gap junction channel at 3.5 Å resolution. *Nature* **458**, 597-602 (2009).

6. Bennett, B.C. et al. An electrostatic mechanism for Ca(2+)-mediated regulation of gap junction channels. *Nat Commun* **7**, 8770 (2016).
7. Myers, J.B. et al. Structure of native lens connexin 46/50 intercellular channels by cryo-EM. *Nature* **564**, 372-377 (2018).
8. Flores, J.A. et al. Connexin-46/50 in a dynamic lipid environment resolved by CryoEM at 1.9 Å. *Nat Commun* **11**, 4331 (2020).
9. Lee, H.J. et al. Cryo-EM structure of human Cx31.3/GJC3 connexin hemichannel. *Sci Adv* **6**, eaba4996 (2020).
10. Kumar, N.M. & Gilula, N.B. The gap junction communication channel. *Cell* **84**, 381-8 (1996).
11. Alexander, D.B. & Goldberg, G.S. Transfer of biologically important molecules between cells through gap junction channels. *Curr Med Chem* **10**, 2045-58 (2003).
12. Lin, L.C. et al. Downregulated myocardial connexin 43 and suppressed contractility in rabbits subjected to a cholesterol-enriched diet. *Lab Invest* **85**, 1224-37 (2005).
13. Plotkin, L.I., Speacht, T.L. & Donahue, H.J. Cx43 and mechanotransduction in bone. *Curr Osteoporos Rep* **13**, 67-72 (2015).
14. Xu, H. et al. Connexin 43 channels are essential for normal bone structure and osteocyte viability. *J Bone Miner Res* **30**, 436-48 (2015).
15. Batra, N. et al. Mechanical stress-activated integrin alpha5beta1 induces opening of connexin 43 hemichannels. *Proc Natl Acad Sci U S A* **109**, 3359-64 (2012).
16. Zhang, X.F. & Cui, X. Connexin 43: Key roles in the skin. *Biomed Rep* **6**, 605-611 (2017).
17. Xing, L., Yang, T., Cui, S. & Chen, G. Connexin Hemichannels in Astrocytes: Role in CNS Disorders. *Front Mol Neurosci* **12**, 23 (2019).
18. Ribeiro-Rodrigues, T.M., Martins-Marques, T., Morel, S., Kwak, B.R. & Girão, H. Role of connexin 43 in different forms of intercellular communication - gap junctions, extracellular vesicles and tunnelling nanotubes. *J Cell Sci* **130**, 3619-3630 (2017).
19. Srinivas, M., Verselis, V.K. & White, T.W. Human diseases associated with connexin mutations. *Biochim Biophys Acta Biomembr* **1860**, 192-201 (2018).
20. Liu, S. et al. Distinct cardiac malformations caused by absence of connexin 43 in the neural crest and in the non-crest neural tube. *Development* **133**, 2063-73 (2006).

21. Kajiwara, Y. et al. GJA1 (connexin43) is a key regulator of Alzheimer's disease pathogenesis. *Acta Neuropathol Commun* **6**, 144 (2018).
22. Kawasaki, A. et al. Modulation of connexin 43 in rotenone-induced model of Parkinson's disease. *Neuroscience* **160**, 61-8 (2009).
23. Aasen, T. et al. Connexins in cancer: bridging the gap to the clinic. *Oncogene* **38**, 4429-4451 (2019).
24. Chen, Q. et al. Carcinoma-astrocyte gap junctions promote brain metastasis by cGAMP transfer. *Nature* **533**, 493-498 (2016).
25. Sinyuk, M., Mulkearns-Hubert, E.E., Reizes, O. & Lathia, J. Cancer Connectors: Connexins, Gap Junctions, and Communication. *Front Oncol* **8**, 646 (2018).
26. Luo, B. et al. Connexin 43 reduces susceptibility to sympathetic atrial fibrillation. *Int J Mol Med* **42**, 1125-1133 (2018).
27. Peracchia, C. Chemical gating of gap junction channels; roles of calcium, pH and calmodulin. *Biochim Biophys Acta* **1662**, 61-80 (2004).
28. Bukauskas, F.F. & Verselis, V.K. Gap junction channel gating. *Biochim Biophys Acta* **1662**, 42-60 (2004).
29. Locke, D. & Harris, A.L. Connexin channels and phospholipids: association and modulation. *BMC Biol* **7**, 52 (2009).
30. Sahu, G. & Bera, A.K. Contribution of intracellular calcium and pH in ischemic uncoupling of cardiac gap junction channels formed of connexins 43, 40, and 45: a critical function of C-terminal domain. *PLoS One* **8**, e60506 (2013).
31. Xu, Q. et al. Gating of connexin 43 gap junctions by a cytoplasmic loop calmodulin binding domain. *Am J Physiol Cell Physiol* **302**, C1548-56 (2012).
32. Shao, Q. et al. Structure and functional studies of N-terminal Cx43 mutants linked to oculodentodigital dysplasia. *Mol Biol Cell* **23**, 3312-21 (2012).
33. Xu, Q., Lin, X., Matiukas, A., Zhang, X. & Veenstra, R.D. Specificity of the connexin W3/4 locus for functional gap junction formation. *Channels (Austin)* **10**, 453-65 (2016).
34. Gemel, J., Lin, X., Veenstra, R.D. & Beyer, E.C. N-terminal residues in Cx43 and Cx40 determine physiological properties of gap junction channels, but do not influence heteromeric assembly with each other or with Cx26. *J Cell Sci* **119**, 2258-68 (2006).

35. Unger, V.M., Kumar, N.M., Gilula, N.B. & Yeager, M. Expression, two-dimensional crystallization, and electron cryo-crystallography of recombinant gap junction membrane channels. *J Struct Biol* **128**, 98-105 (1999).
36. Oshima, A., Tani, K., Hiroaki, Y., Fujiyoshi, Y. & Sosinsky, G.E. Three-dimensional structure of a human connexin26 gap junction channel reveals a plug in the vestibule. *Proc Natl Acad Sci U S A* **104**, 10034-9 (2007).
37. Oshima, A. et al. Asymmetric configurations and N-terminal rearrangements in connexin26 gap junction channels. *J Mol Biol* **405**, 724-35 (2011).
38. Khan, A.K. et al. A Steric "Ball-and-Chain" Mechanism for pH-Mediated Regulation of Gap Junction Channels. *Cell Rep* **31**, 107482 (2020).
39. Swietach, P., Rossini, A., Spitzer, K.W. & Vaughan-Jones, R.D. H⁺ ion activation and inactivation of the ventricular gap junction: a basis for spatial regulation of intracellular pH. *Circ Res* **100**, 1045-54 (2007).
40. Garcarena, C.D., Malik, A., Swietach, P., Moreno, A.P. & Vaughan-Jones, R.D. Distinct moieties underlie biphasic H⁽⁺⁾ gating of connexin43 channels, producing a pH optimum for intercellular communication. *FASEB J* **32**, 1969-1981 (2018).
41. Duffy, H.S. et al. pH-dependent intramolecular binding and structure involving Cx43 cytoplasmic domains. *J Biol Chem* **277**, 36706-14 (2002).
42. Hirst-Jensen, B.J., Sahoo, P., Kieken, F., Delmar, M. & Sorgen, P.L. Characterization of the pH-dependent interaction between the gap junction protein connexin43 carboxyl terminus and cytoplasmic loop domains. *J Biol Chem* **282**, 5801-13 (2007).
43. Voegtli, W.C., White, D.J., Reiter, N.J., Rusnak, F. & Rosenzweig, A.C. Structure of the bacteriophage lambda Ser/Thr protein phosphatase with sulfate ion bound in two coordination modes. *Biochemistry* **39**, 15365-74 (2000).
44. Schlieker, C. et al. Structure of a herpesvirus-encoded cysteine protease reveals a unique class of deubiquitinating enzymes. *Mol Cell* **25**, 677-87 (2007).
45. Penkov, N.V. & Penkova, N. Key Differences of the Hydrate Shell Structures of ATP and Mg.ATP Revealed by Terahertz Time-Domain Spectroscopy and Dynamic Light Scattering. *J Phys Chem B* **125**, 4375-4382 (2021).
46. Roh, S.H. et al. Subunit conformational variation within individual GroEL oligomers resolved by Cryo-EM. *Proc Natl Acad Sci U S A* **114**, 8259-8264 (2017).

47. Huang, J. et al. CHARMM36m: an improved force field for folded and intrinsically disordered proteins. *Nat Methods* **14**, 71-73 (2017).
48. Yoo, J. & Aksimentiev, A. New tricks for old dogs: improving the accuracy of biomolecular force fields by pair-specific corrections to non-bonded interactions. *Phys Chem Chem Phys* **20**, 8432-8449 (2018).
49. Yoo, J. & Aksimentiev, A. Improved Parameterization of Amine-Carboxylate and Amine-Phosphate Interactions for Molecular Dynamics Simulations Using the CHARMM and AMBER Force Fields. *J Chem Theory Comput* **12**, 430-43 (2016).
50. Dydowiczová, A., Brózman, O., Babica, P. & Sovadinová, I. Improved multiparametric scrape loading-dye transfer assay for a simultaneous high-throughput analysis of gap junctional intercellular communication, cell density and viability. *Sci Rep* **10**, 730 (2020).
51. Paznekas, W.A. et al. GJA1 mutations, variants, and connexin 43 dysfunction as it relates to the oculodentodigital dysplasia phenotype. *Hum Mutat* **30**, 724-33 (2009).
52. Yoo, J. & Aksimentiev, A. Molecular Dynamics of Membrane-Spanning DNA Channels: Conductance Mechanism, Electro-Osmotic Transport, and Mechanical Gating. *J Phys Chem Lett* **6**, 4680-7 (2015).
53. Mim, C., Perkins, G. & Dahl, G. Structure versus function: Are new conformations of pannexin 1 yet to be resolved? *J Gen Physiol* **153**, e202012754 (2021).
54. Burendei, B. et al. Cryo-EM structures of undocked innexin-6 hemichannels in phospholipids. *Sci Adv* **6**, eaax3157 (2020).
55. Nguyen, T.A. et al. Functional Anatomy of the Human Microprocessor. *Cell* **161**, 1374-87 (2015).
56. Lee, H.J. et al. Cryo-EM structure of human Cx31.3/GJC3 connexin hemichannel. *Sci Adv* **6**, eaba4996 (2020).
57. Ritchie, T.K. et al. Chapter 11 - Reconstitution of membrane proteins in phospholipid bilayer nanodiscs. *Methods Enzymol* **464**, 211-31 (2009).
58. Zivanov, J. et al. New tools for automated high-resolution cryo-EM structure determination in RELION-3. *Elife* **7**(2018).
59. Punjani, A., Rubinstein, J.L., Fleet, D.J. & Brubaker, M.A. cryoSPARC: algorithms for rapid unsupervised cryo-EM structure determination. *Nat Methods* **14**, 290-296 (2017).
60. Zheng, S.Q. et al. MotionCor2: anisotropic correction of beam-induced motion for improved cryo-electron microscopy. *Nat Methods* **14**, 331-332 (2017).

61. Zhang, K. Gctf: Real-time CTF determination and correction. *J Struct Biol* **193**, 1-12 (2016).
62. Zivanov, J., Nakane, T. & Scheres, S.H.W. A Bayesian approach to beam-induced motion correction in cryo-EM single-particle analysis. *IUCrJ* **6**, 5-17 (2019).
63. Zivanov, J., Nakane, T. & Scheres, S.H.W. Estimation of high-order aberrations and anisotropic magnification from cryo-EM data sets in RELION-3.1. *IUCrJ* **7**, 253-267 (2020).
64. Scheres, S.H. & Chen, S. Prevention of overfitting in cryo-EM structure determination. *Nat Methods* **9**, 853-4 (2012).
65. Kucukelbir, A., Sigworth, F.J. & Tagare, H.D. Quantifying the local resolution of cryo-EM density maps. *Nat Methods* **11**, 63-5 (2014).
66. Bepler, T. et al. Positive-unlabeled convolutional neural networks for particle picking in cryo-electron micrographs. *Nat Methods* **16**, 1153-1160 (2019).
67. Roh, S.H. et al. Subunit conformational variation within individual GroEL oligomers resolved by Cryo-EM. *Proc Natl Acad Sci U S A* **114**, 8259-8264 (2017).
68. Gestaut, D. et al. The Chaperonin TRiC/CCT Associates with Prefoldin through a Conserved Electrostatic Interface Essential for Cellular Proteostasis. *Cell* **177**, 751-765 e15 (2019).
69. Emsley, P., Lohkamp, B., Scott, W.G. & Cowtan, K. Features and development of Coot. *Acta Crystallogr D Biol Crystallogr* **66**, 486-501 (2010).
70. Casañal, A., Lohkamp, B. & Emsley, P. Current developments in Coot for macromolecular model building of Electron Cryo-microscopy and Crystallographic Data. *Protein Sci* **29**, 1069-1078 (2020).
71. Afonine, P.V. et al. Real-space refinement in PHENIX for cryo-EM and crystallography. *Acta Crystallogr D Struct Biol* **74**, 531-544 (2018).
72. Moriarty, N.W., Grosse-Kunstleve, R.W. & Adams, P.D. electronic Ligand Builder and Optimization Workbench (eLBOW): a tool for ligand coordinate and restraint generation. *Acta Crystallogr D Biol Crystallogr* **65**, 1074-80 (2009).
73. Waterhouse, A. et al. SWISS-MODEL: homology modelling of protein structures and complexes. *Nucleic Acids Res* **46**, W296-W303 (2018).
74. Flores, J.A. et al. Connexin-46/50 in a dynamic lipid environment resolved by CryoEM at 1.9 Å. *Nat Commun* **11**, 4331 (2020).
75. Williams, C.J. et al. MolProbity: More and better reference data for improved all-atom structure validation. *Protein Sci* **27**, 293-315 (2018).

76. Smart, O.S., Neduvelil, J.G., Wang, X., Wallace, B.A. & Sansom, M.S. HOLE: a program for the analysis of the pore dimensions of ion channel structural models. *J Mol Graph* **14**, 354-60, 376 (1996).
77. Chovancova, E. et al. CAVER 3.0: a tool for the analysis of transport pathways in dynamic protein structures. *PLoS Comput Biol* **8**, e1002708 (2012).
78. Abraham, M.J. et al. GROMACS: High performance molecular simulations through multi-level parallelism from laptops to supercomputers. *SoftwareX* **1-2**, 19-28 (2015).
79. Huang, J. et al. CHARMM36m: an improved force field for folded and intrinsically disordered proteins. *Nat Methods* **14**, 71-73 (2017).
80. Yoo, J. & Aksimentiev, A. New tricks for old dogs: improving the accuracy of biomolecular force fields by pair-specific corrections to non-bonded interactions. *Phys Chem Chem Phys* **20**, 8432-8449 (2018).
81. Parrinello, M. & Rahman, A. Polymorphic transitions in single crystals: A new molecular dynamics method. *J Appl Phys* **52**, 7182-7190 (1981).
82. Nosé, S. & Klein, M.L. Constant pressure molecular dynamics for molecular systems. *Molecular Physics* **50**, 1055-1076 (1983).
83. Darden, T., York, D. & Pedersen, L. Particle mesh Ewald: An N·log(N) method for Ewald sums in large systems. *J Chem Phys* **98**, 10089-10092 (1993).
84. Hess, B., Bekker, H., Berendsen, H.J.C. & Fraaije, J.G.E.M. LINCS: A linear constraint solver for molecular simulations. *J Comput Chem* **18**, 1463-1472 (1997).
85. Miyamoto, S. & Kollman, P.A. Settle: An analytical version of the SHAKE and RATTLE algorithm for rigid water models. *J Comput Chem* **13**, 952-962 (1992).
86. Yoo, J. & Aksimentiev, A. Molecular Dynamics of Membrane-Spanning DNA Channels: Conductance Mechanism, Electro-Osmotic Transport, and Mechanical Gating. *J Phys Chem Lett* **6**, 4680-7 (2015).
87. el-Fouly, M.H., Trosko, J.E. & Chang, C.C. Scrape-loading and dye transfer. A rapid and simple technique to study gap junctional intercellular communication. *Exp Cell Res* **168**, 422-30 (1987).
88. Tahrir, G.F. et al. Role of Bcl2-associated Athanogene 3 in Turnover of Gap Junction Protein, Connexin 43, in Neonatal Cardiomyocytes. *Sci Rep* **9**, 7658 (2019).

Table 1

Table 1 | Cryo-EM data collection, refinement and validation statistics.

	Cx43-WT (pH 8.0)		Cx43-M257 (pH 8.0)
	In detergents	In nanodiscs	In detergents
	EMD-31495	EMD-31496	EMD-31497
	PDB 7F92	PDB 7F93	PDB 7F94
Data collection and processing			
Magnification	96,000	120,000	96,000
Voltage (kV)	300	300	300
Electron exposure (e ⁻ /Å ²)	40	40	40
Defocus range (μm)	-1.25 ~ -2.75	-1.25 ~ -2.75	-1.25 ~ -2.75
Pixel size (Å)	0.675	0.5235	0.675
Software	RELION 3.1	cryoSPARC 3.1	RELION 3.1
Symmetry imposed	D6	D6	C6
Initial particle images (no.)	1,130,417	1,683,178	559,754
Final particle images (no.)	21,689	28,341	7,446
Overall map resolution (Å)			
FSC threshold 0.143	3.1	3.6	3.6
Map sharpening <i>B</i> factor (Å ²)	-38.129	-122.3	N/A
Refinement			
Initial model used (PDB code)	<i>De novo</i>	7F92	7F92 & 7JKC
Model resolution (Å)			
FSC threshold 0.5	3.1	3.9	3.5
Model composition			
Non-hydrogen atoms	21,408	20,808	19,182
Protein residues	2,352	2,352	2,358
Ligands	MC3 : 144	MC3 : 120	N/A
<i>B</i> factors (Å ²)			
Protein	29.82	121.14	129.88
Ligand	46.40	114.90	N/A

R.m.s. deviations			
Bond lengths (Å)	0.008	0.007	0.008
Bond angles (°)	1.126	1.228	1.024
Validation			
MolProbity score	0.87	1.66	1.52
Clash score	0.63	3.40	2.40
Poor rotamers (%)	1.14	3.43	1.71
Ramachandran plot			
Favored (%)	97.40	97.40	95.32
Allowed (%)	2.60	2.60	4.42
Disallowed (%)	0	0	0.26

Figures

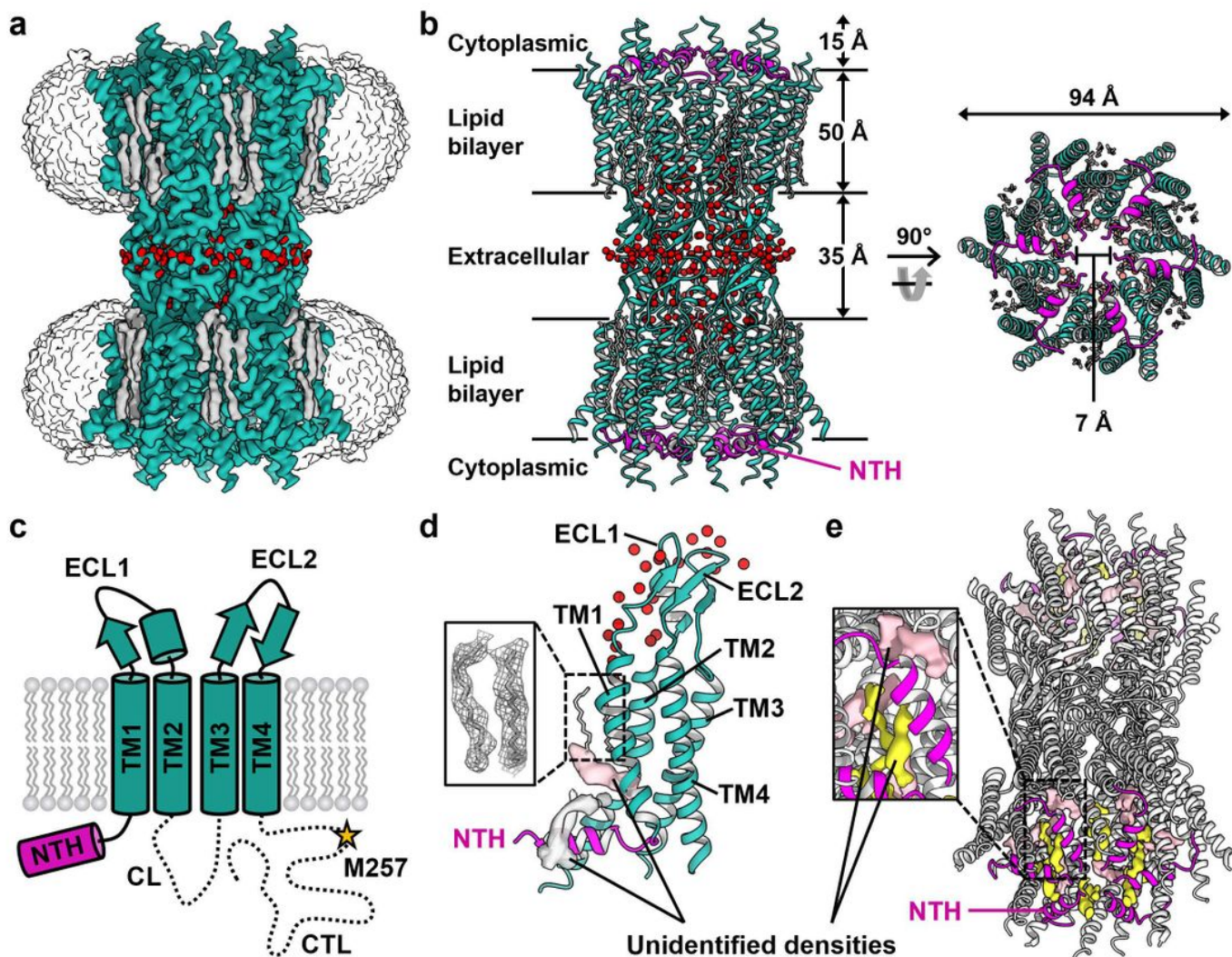


Figure 1

Structure of Cx43-WT GJIC at pH 8.0 in gate-covering NTH (GCN) conformation. a, Cryo-EM reconstruction map of Cx43-WT GJIC surrounded by detergent micelles. Map densities for protein and water molecules are colored in green and red, respectively. b, Ribbon representation of the Cx43-WT GJIC structure viewed from the membrane (left) and the cytoplasm (right). NTHs are colored in magenta. Water molecules are shown as red spheres. c, Topology cartoon of Cx43 protomer. Dashed lines indicate flexible loops that could not be structurally determined. M257 residue is marked and labeled. d, Ribbon representation of a single protomer structure. Acyl chains originated from detergents or lipids are shown in a box. Two unidentified map densities presumed to be CHS (pink) and a part of LMNG (gray) are shown. e, Ribbon representation of the Cx43-WT GJIC structure in lipid nanodiscs at pH 8.0. NTHs are colored in magenta. Unidentified map densities presumed to be CHSs (pink) and parts of phospholipids (yellow) are shown. The close-up view of the indicated region of the cytoplasmic gate is shown in a box.

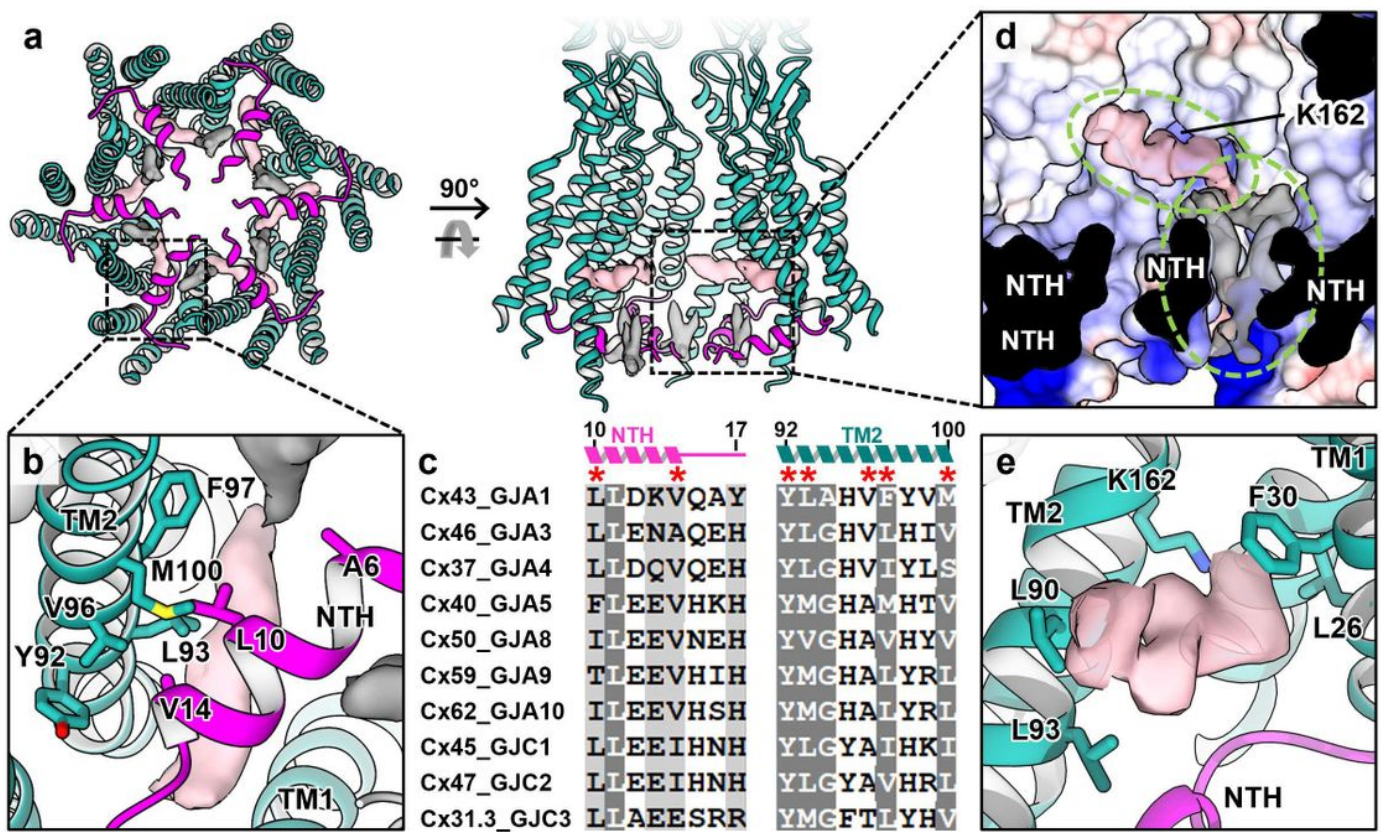


Figure 2

Intramolecular NTH-TM2 interaction and lipid/detergent-binding stabilize the GCN conformation. a, Structure of Cx43-WT GJICH in LMNG/CHS at pH 8.0 in the GCN conformation. Map densities presumed to be CHSs (pink) and lipids/detergents (gray) are shown. b, Detailed intramolecular hydrophobic interactions between NTH and TM2. Seven residues involved in the interaction are drawn as sticks and labeled. A6 residue is also represented and labeled to show its location far from TM2. c, Sequence alignment of A and C class connexins. More than 90% and 80% similarly conserved residues are shaded in dark gray and light gray, respectively. The residues involved in intramolecular NTH-TM2 interaction are indicated by asterisks. d,e, Close-up views of map densities presumed to be CHS (pink) and phospholipid/detergent (gray). (d) Map densities are indicated by green dotted circles. The protein surface is colored according to the electrostatic potential from red (-10 kT/e) to blue (+10 kT/e). (e) The hydrophobic pocket formed by NTH, TM1 and TM2 embeds the sterol-like density. The pocket-forming residues are represented as sticks and labeled.

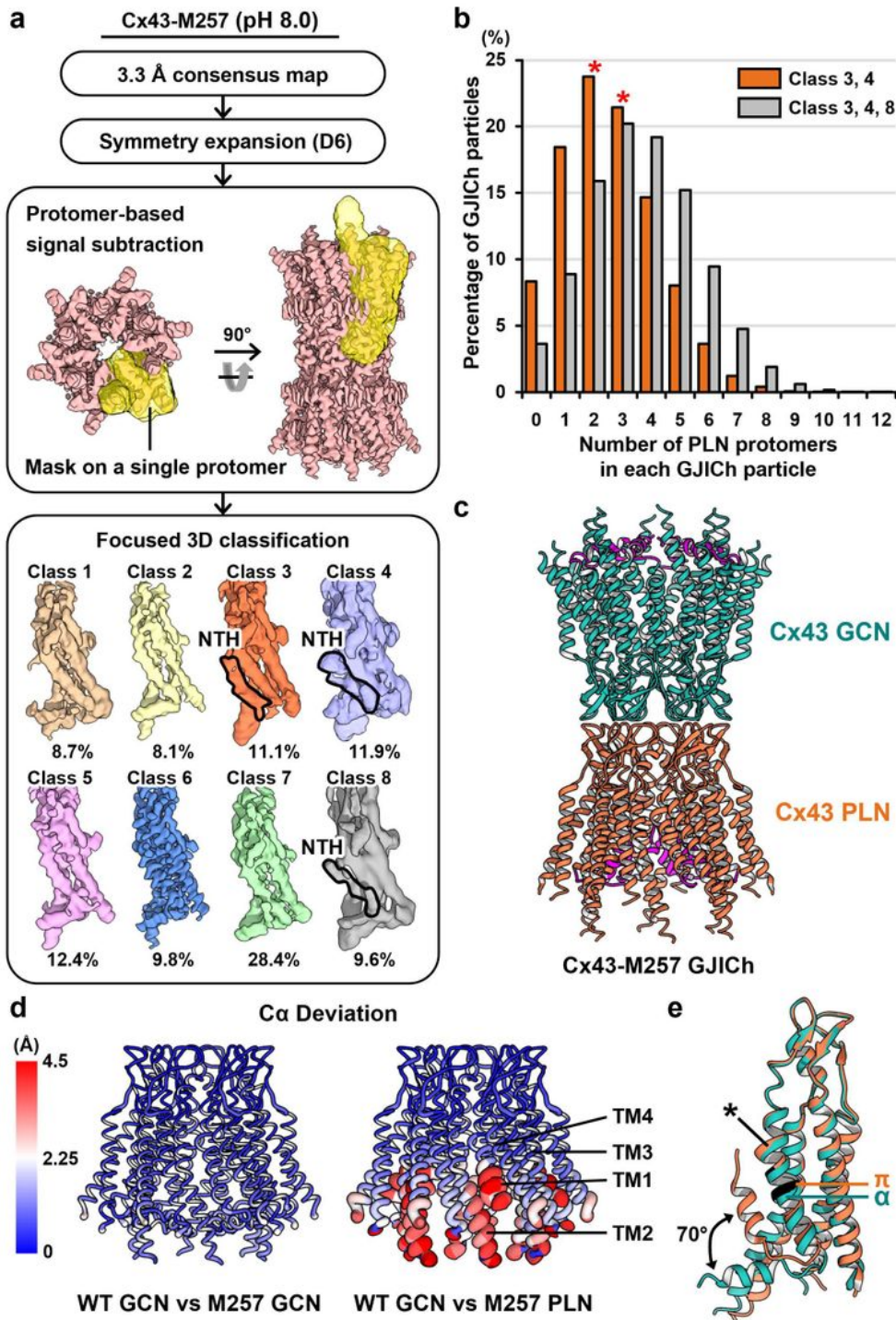


Figure 3

Structural analyses of Cx43-M257 GJCh. a, Workflow of the single protomer-based conformational variation analysis using the Cx43-M257 GJCh dataset. See Methods for detailed description. The densities of NTHs in the PLN conformation are highlighted by black bold lines. b, Distribution of various compositions of PLN protomers within GJCh particles. The number of GJCh particles with each number of PLN protomers from 0 to 12 was analyzed using classes 3 and 4 (orange bars) or classes 3, 4, and 8

(gray bars) in a. c, Structure of Cx43-M257 GJICh containing fully GCN hemichannel (green) on one side and fully PLN hemichannel (orange) on the other side. d, Structural alignments of Cx43-WT hemichannel (GCN conformation) with Cx43-M257 hemichannels in GCN (left) and PLN (right) conformations. Ca deviation of each residue is colored according to the range bar on the left. NTHs are not included in the calculation of Ca deviation. e, Superposition of GCN and PLN protomers of Cx43-WT and Cx43-M257 GJIChs, respectively. The conformational shift of NTH is indicated by a two-way arrow. α - and π -helices in the middle of TM1 are indicated and labelled. Asterisk indicates another π -helix in the extracellular end of TM1, which is not changed between GCN and PLN conformations.

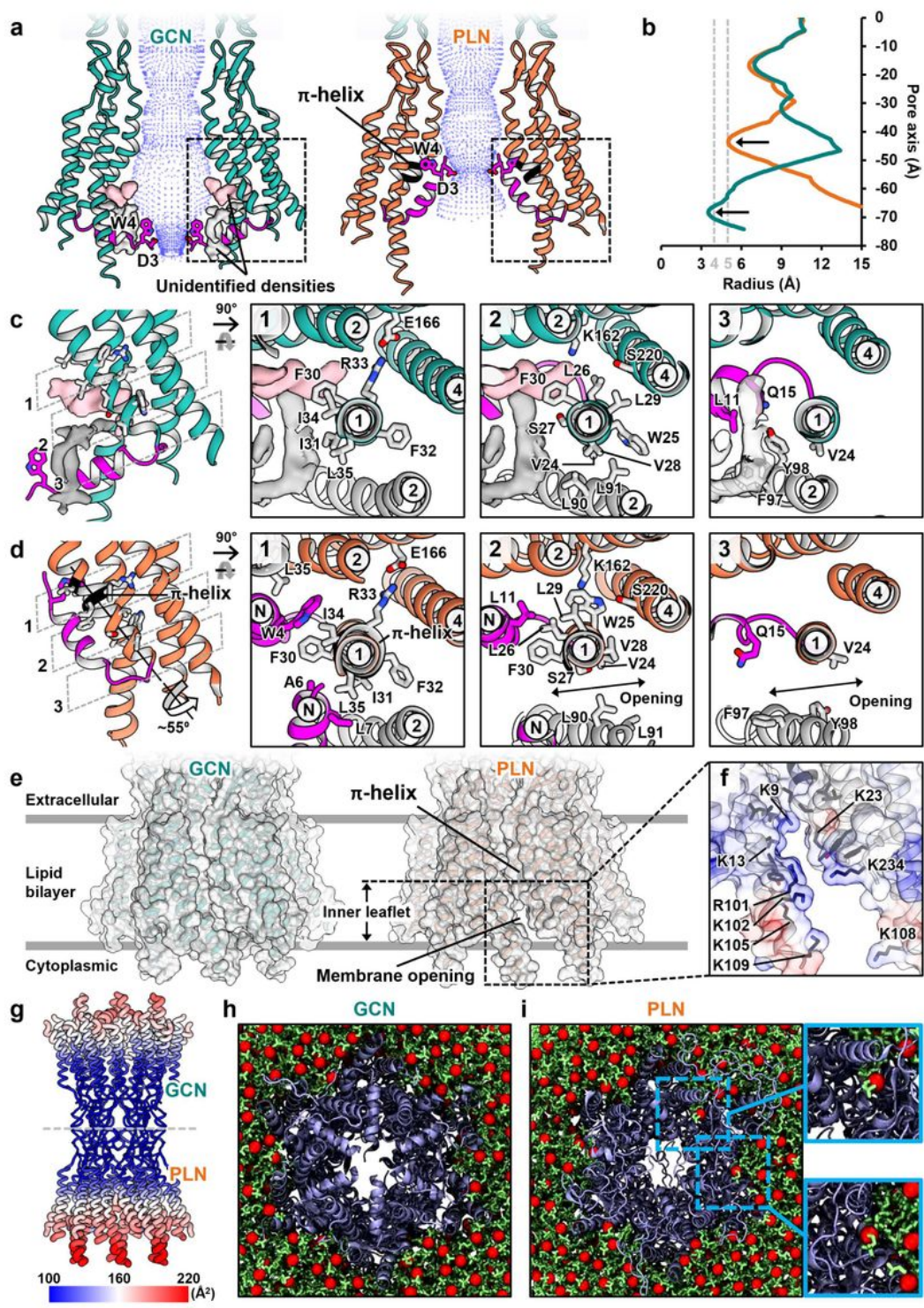


Figure 4

Structural details of the GCN-to-PLN transition, π -helix formation in the middle of TM1 and the membrane opening between TMDs. a, Comparison between GCN and PLN conformations depicted with pore pathways. Only two protomers facing each other are shown for clarity. NTHs are colored in magenta. π -helix in the middle of TM1 is colored in black and labeled. b, Comparison between the solvent-accessible pore radii changing along the pore pathways of GCN and PLN hemichannels. c,d, Detailed structural

comparison between GCN (c) and PLN (d) protomers at the regions boxed in a. All residues in the cytoplasmic half of TM1 including π -helix-forming residues but only a selected few residues are represented as gray sticks in TMs and magenta sticks in NTHs, and labeled for clarity. GCN and PLN protomers were cross-sectioned at three levels (gray dotted lines) along the helical axis of TM1, and individually viewed from the extracellular side. TM2 in a neighboring protomer is colored in gray. Circled numbers and 'N' indicate the TM helix numbers and NTH, respectively. e, Surface representations of fully GCN and PLN hemichannels. The membrane opening is shown only in PLN hemichannel. f, Electrostatic surface potential of the membrane opening. On a transparent surface of the intermolecular interface, the electrostatic potential is colored from red (-10 kT/e) to blue (+10 kT/e). Positively charged side chains are shown as sticks and labeled. Hydrophobic residues are also drawn as sticks but not labeled. g, Atomic displacement parameter (B-factor) distribution in the structure of Cx43-M257 GJCh containing fully GCN hemichannel on one side and fully PLN hemichannel on the other side. h,i, MD simulations show the lateral movement of lipid molecules through membrane openings in fully PLN GJCh (i), but not in fully GCN GJCh (h). Close-up views of membrane openings between protomers are shown in boxes.

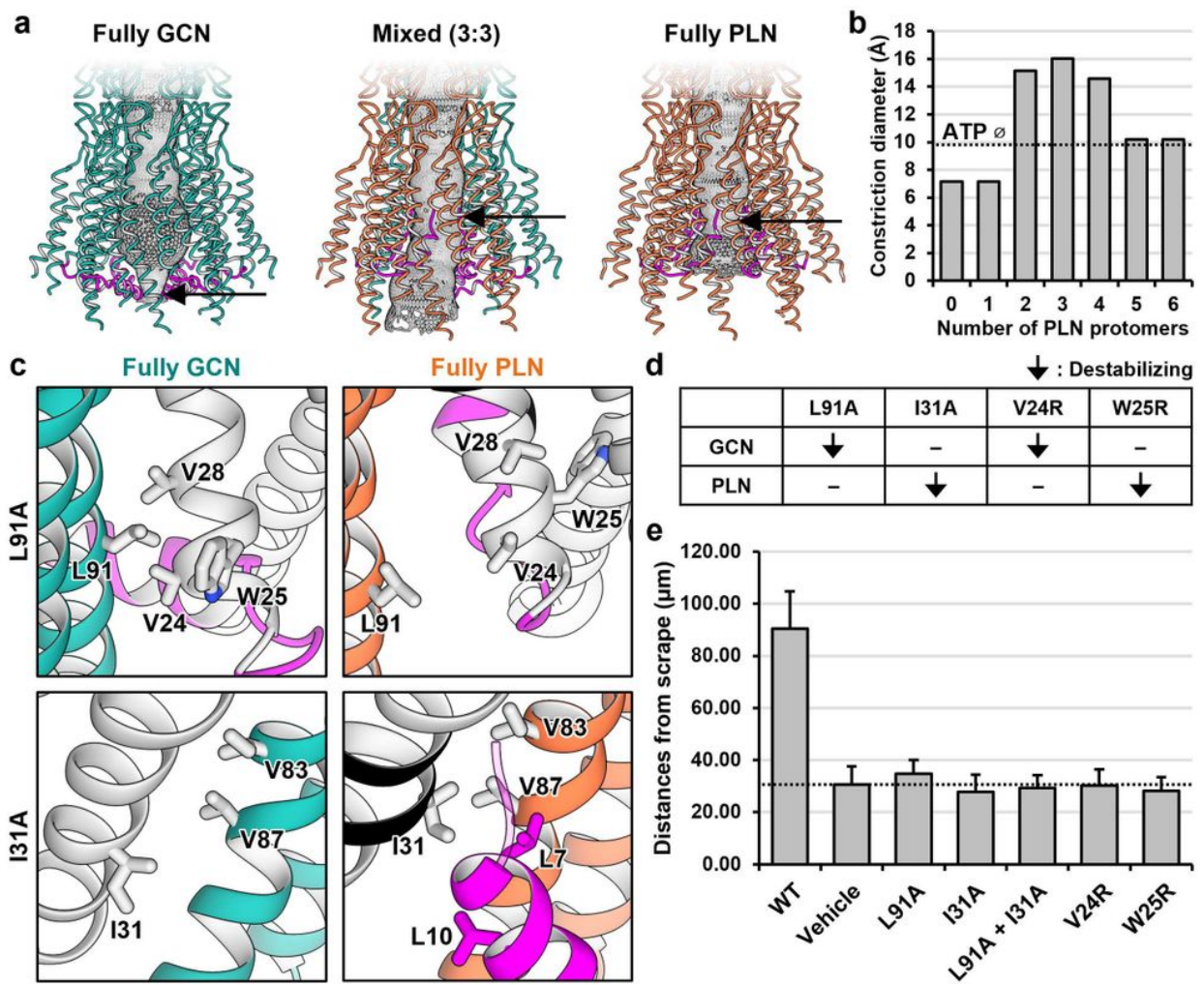


Figure 5

Conformational changes in NTH and TM1 are crucial for the transport of large molecules. a, Comparison of the pore pathways in fully GCN, 3:3 mixed (three consecutive PLN and GCN), and fully PLN hemichannels. Black arrows indicate constriction sites. b, Constriction diameters of various hemichannels with 0 to 6 consecutive PLN protomer(s). The hydrodynamic diameter of ATP (9.8 Å) is indicated by a black dashed line. c, Rationale design of L91A and I31A mutations disturbing GCN and PLN conformations, respectively, but not the other way around. d, The expected effects of the indicated mutations on Cx43 conformations are shown in the table. e, The inhibitory effects of Cx43 mutations on dye transfer activity in HEK293E cells. Bar graphs show the maximum distances of dye transfer from scrape lines through the indicated Cx43 mutant GJICs. Data are presented as the mean \pm S.D. (n = 9).

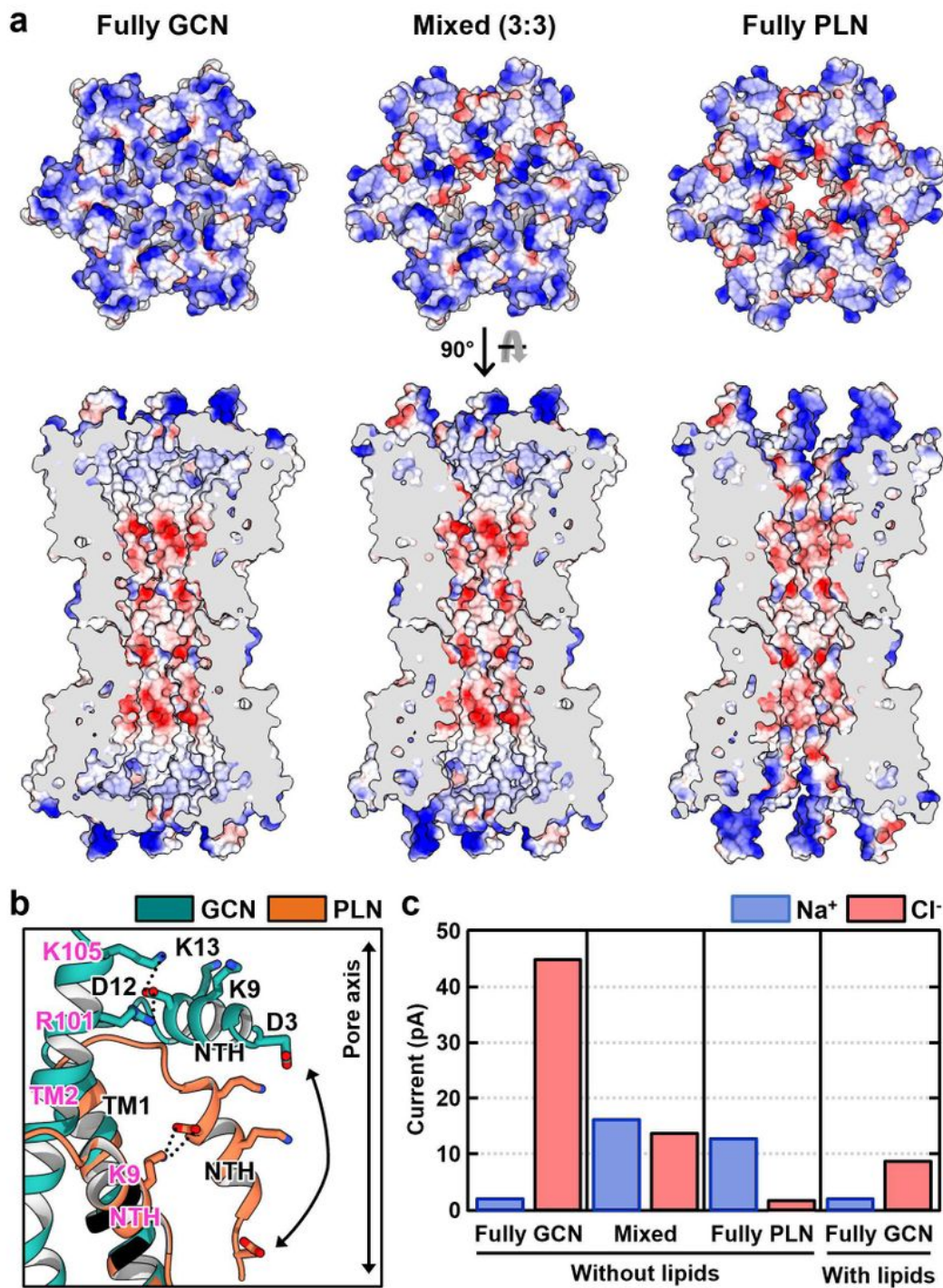


Figure 6

Ion selectivity among fully GCN, mixed, and fully PLN GJICs. a, Electrostatic surface potentials of fully GCN, 3:3 mixed, and fully PLN models viewed from the cytoplasm (top) and the membrane (bottom). b, GCN and PLN protomers were superposed. Only NTHs, TM1s and TM2s are represented for clarity. Asp3, Lys9, Asp12, and Lys13 in NTHs are shown as sticks and labeled. Interacting residues in the neighboring

protomers are also shown as sticks and colored in magenta. c, Ionic currents and selectivities of three different GJCh conformations in a.

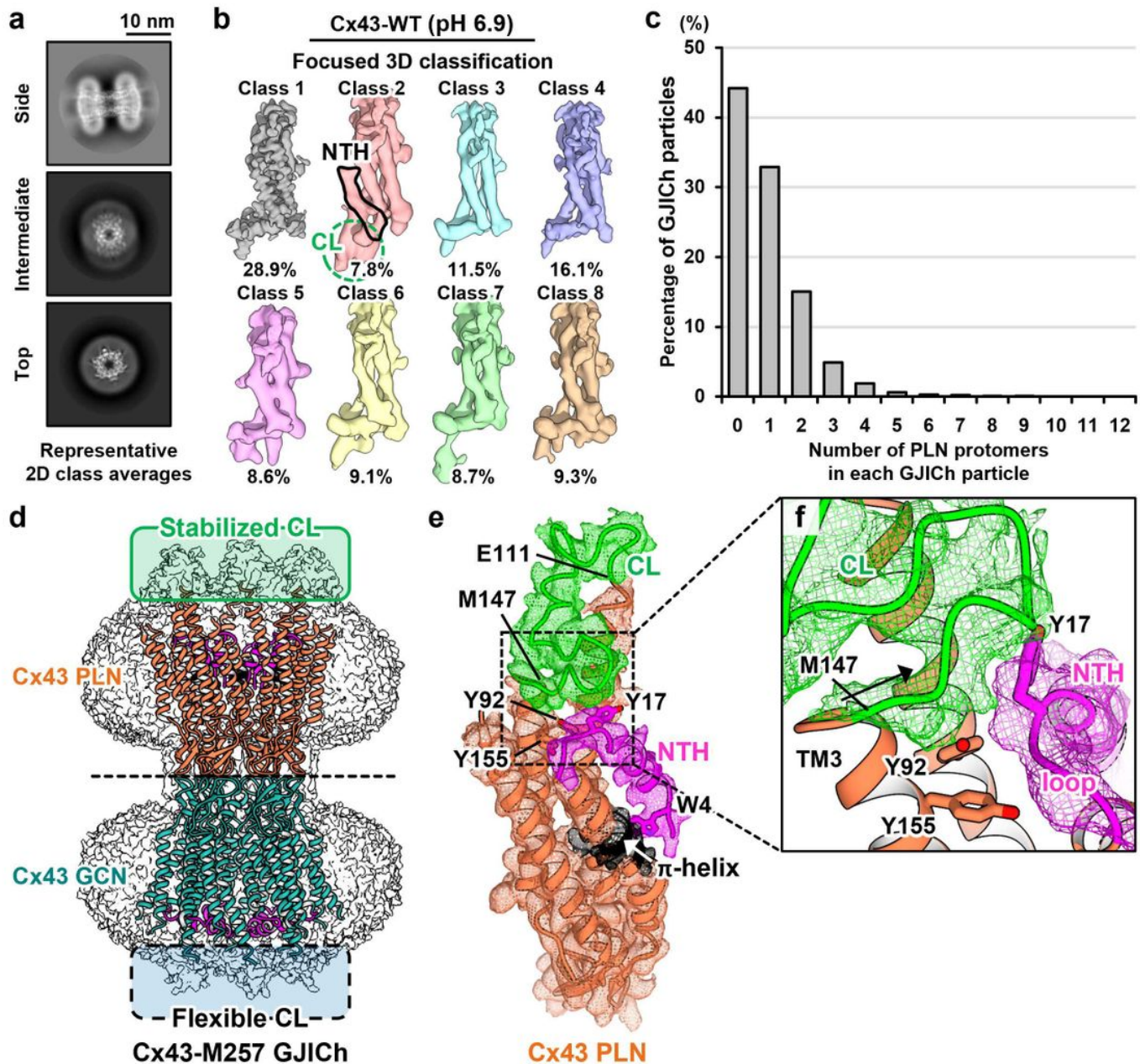


Figure 7

Identification of PLN protomers in Cx43-WT GJICs at pH 6.9 and stabilization of the CL in the PLN conformation. a, Three representative 2D class averages of Cx43-WT GJIC at pH 6.9. b, Single protomer-based conformational variation analysis using the dataset of Cx43-WT GJIC at pH 6.9. The densities of NTH and CL in Class 2 in the PLN conformation are indicated by a black bold line and a green circle, respectively. c, Distribution of various compositions of PLN protomers within GJIC particles. d, Strong map densities of CLs observed in fully PLN hemichannel (orange) of Cx43-M257 GJIC, but not in fully

GCN hemichannel (green). e, The ribbon model of Cx43 in the PLN conformation is shown with its cryo-EM map density (mesh). NTH, CL, π -helix and the rest are colored in magenta, green, black and orange, respectively. f, Close-up view of the region boxed in e. Met147 is indicated with black line where the CL ends. Tyr17 in the loop connecting NTH and TM1, Tyr92 in TM2 and Tyr155 in TM3 located at the CL-loop interface are drawn as sticks and labeled.

Supplementary Files

This is a list of supplementary files associated with this preprint. Click to download.

- [video1pihelixfig4.mp4](#)
- [video2NTHlinkerfigS6.mp4](#)
- [video3membraneopeningfig4.mp4](#)
- [video4MDPLNfig4.mp4](#)
- [video5MDGCNfig4.mp4](#)
- [video6NTHgatingfigS7.mp4](#)
- [ExtendedDataFiguresXLegends.pdf](#)